Astrocyte redox dysregulation causes prefrontal hypoactivity: sulforaphane treats non-ictal pathophysiology in ALDH7A1-mediated epilepsy — Source link ↗

Travis E. Faust, Wendy Xin, Wendy Xin, Brian K. Lee ...+13 more authors

Institutions: Johns Hopkins University, National Institute on Drug Abuse, Heidelberg University, Johns Hopkins University School of Medicine

Topics: Knockout mouse

Related papers:

- Neuronal Calcium Imaging, Excitability, and Plasticity Changes in the Aldh2-/- Mouse Model of Sporadic Alzheimer's Disease.

- Author response: Novel ALDH5A1 variants and genotype: Phenotype correlation in SSADH deficiency

- Potential Roles of Redox Dysregulation in the Development of Schizophrenia.

- Insulin regulates astrocyte gliotransmission and modulates behavior

- 2.5 Redox Dysregulation in Schizophrenia: Genetic Susceptibility and Pathophysiological Mechanisms

Share this paper: 👍 🐦 in ✉️

View more about this paper here: https://typeset.io/papers/astrocyte-redox-dysregulation-causes-prefrontal-hypoactivity-2vc8c9r4h3

Astrocyte redox dysregulation causes prefrontal hypoactivity: sulforaphane treats non-ictal pathophysiology in ALDH7A1-mediated epilepsy

Travis E. Faust[1,2], Wendy Xin[1,3], Brian Lee[2], Amit Agarwal[1,4], Sneha Saha[2], Trexy Palen[2], Tyler Cash-Padgett[2], Daniel Wood[2], Antonello Bonci[1,3], Jed W. Fahey[5], Hanna Jaaro-Peled[2], Dwight E. Bergles[1,6], Akira Sawa[1,2,7,8,9,10]*

1. Solomon H. Snyder Department of Neuroscience, Johns Hopkins University School of Medicine, Baltimore, MD 21205, USA
2. Department of Psychiatry and Behavioral Sciences, Johns Hopkins University School of Medicine, Baltimore, MD 21205, USA
3. Synaptic Plasticity Section, Cellular Neurobiology Branch, National Institute on Drug Abuse Intramural Research Program, Baltimore, MD 21224, USA
4. The Chica and Heinz Schaller Research Group, Institute for Anatomy and Cell Biology, Heidelberg University, 69120 Heidelberg, Germany
5. Department of Medicine, Division of Clinical Pharmacology, Johns Hopkins University School of Medicine, Baltimore, MD 21205, USA
6. Johns Hopkins University Kavli Neuroscience Discovery Institute, Baltimore, MD 21205, USA
7. Department of Biomedical Engineering, Johns Hopkins University School of Medicine, Baltimore, MD 21205, USA
8. McKusick-Nathans Institute of Genetic Medicine, Johns Hopkins University School of Medicine, Baltimore, MD 21205, USA
9. Department of Mental Health, Johns Hopkins Bloomberg School of Public Health, Baltimore, MD 21205, USA
10. Lead contact

*Correspondence: asawa1@jhmi.edu

Abstract

Mutations in the astrocyte-enriched enzyme aldehyde dehydrogenase 7a1 (ALDH7A1) cause a neonatal epilepsy accompanied by treatment-resistant, inter-ictal neuropsychiatric symptoms. Nevertheless, the mechanistic impact of ALDH7A1 dysfunction in the brain remains elusive. We generated ALDH7A1 knockout mice and report that constitutive global ALDH7A1 depletion increases chemoconvulsant sensitivity and altered mood-associated behaviors. However, contrary to our expectation, astrocyte-specific ALDH7A1 depletion only affects mood-associated behaviors. Accordingly, in astrocyte-specific ALDH7A1 knockout mice, we show enhanced redox-sensitive microdomain Ca^{2+} signaling in astrocytes and both elevated synaptic inhibitory tone and increased dendritic spine density in prelimbic pyramidal neurons. Sulforaphane (SFN), an indirect antioxidant and dietary supplement, has been explored as a possible treatment to ameliorate neuropsychiatric manifestations in autism and schizophrenia, at least at the clinical levels, but its mechanism in the brain is unclear. Here we show that SFN rescues both the physiological and behavioral changes by targeting astrocytic redox imbalance in ALDH7A1 knockout mice, implicating astrocyte redox changes in creating cortical excitatory-inhibitory imbalance and mood alteration.

Patients diagnosed with epilepsy not only suffer from ictal events (seizures), but also from cognitive deficits and other behavioral symptoms in the periods between seizures[1-4]. These non-ictal symptoms represent a major challenge for the treatment of epilepsy, as they can persist even after seizures are controlled. Whole genome sequencing studies have revealed that certain risk factors are shared between epilepsy and other neuropsychiatric disorders, suggesting that the molecular changes that increase seizure risk can also influence cognition and behavior in the absence of seizures[5]. Further evidence from post-mortem studies, human brain imaging, and mouse models suggests that excitatory-inhibitory (E-I) imbalance in specific brain circuits may underlie cognitive and emotional deficits in psychiatric disorders, implying that altered E-I balance could underlie both ictal and non-ictal symptoms in epilepsy[6-8].

To develop novel treatment strategies for sporadic, heterogeneous disorders such as epilepsy, scientists have increasingly turned to rare genetic disorders in which disease etiology can be linked back to a shared biological factor. One such case is pyridoxine-dependent epilepsy (PDE) which is caused by *ALHD7A1* loss-of-function mutations[9]. *ALDH7A1* mutations in PDE cause enzymatic dysfunction of aldehyde dehydrogenase 7a1 (ALDH7A1), leading to the buildup of aldehydes in the lysine degradation pathway that inactivate vitamin B6. In PDE patients, seizures are responsive to vitamin B6 (a.k.a. pyridoxine) supplementation but neurological and behavioral symptoms including developmental delay and cognitive impairments persist into adulthood even after seizures are controlled[10,11]. Dietary lysine restriction is also recommended as an adjunct therapy to vitamin B6 but evidence of its benefits remains limited[12]. Vitamin B6 and lysine restriction treatments are both based on the enzymology of ALDH7A1 *in vitro* and in peripheral tissues, but due to a current lack of mammalian models, it is unknown how ALDH7A1 depletion affects the brain. Understanding the

3

pathophysiology of PDE could allow us to develop more generalized therapies against non-ictal symptoms in PDE that could be extended to other forms of epilepsy or neurocognitive impairment.

ALDH7A1 is one of 19 aldehyde dehydrogenase (ALDH) isoenzymes which oxidize a wide range of endogenous and exogenous aldehydes into carboxylic acids via $NAD(P)^+$-dependent reactions[13] with overlapping substrate specificities[14], providing cells protection against electrophilic stress[15,16,17]. ALDHs also participate in redox homeostasis through regulation of $NAD(P)H$[18] and can act as either direct or indirect antioxidants[19] that protect against oxidative stress caused by excess reactive oxygen species (ROS). Even in the absence of electrophilic/oxidative stress, maintaining redox balance is essential for $NAD(P)H$ and ROS signaling events that coordinate cellular processes that are dependent on metabolic state. In humans, mutations and polymorphisms in ALDH family members genes cause metabolic disorders and diseases that are often accompanied by neuropsychiatric symptoms[20], suggesting that ALDH activity may serve a generalized function in the brain.

Within the brain, ALDH7A1 and the ALDH family at large are preferentially enriched in astrocytes[21] and the ALDH1L1 isoenzyme is widely used as an astrocyte cell identity marker[22,23]. Astrocytes are principally responsible for brain homeostatic functions to support other brain cells, particularly neurons[24]. In addition to metabolic functions, astrocytes influence neuronal activity through regulation of synaptogenesis, synaptic strength, neuronal excitability, and extracellular levels of ions and neurotransmitters, all of which can influence E-I balance[25,26]. However, despite the abundance and enrichment of ALDHs in astrocytes, the biological significance of this expression pattern remains unexplored.

To investigate the neurobiology of ALDH7A1 deficiency, we generated a conditional knockout mouse for ALDH7A1. Behavioral testing of mice with constitutive global depletion of ALDH7A1 revealed both an increased seizure susceptibility and non-ictal behavioral alterations. Subsequent protein analysis confirmed that the majority of ALDH7A1 is expressed in astrocytes in the postnatal brain. However, in mice with perinatal *Aldh7a1* deletion specifically in astrocytes, we observed behavioral deficits in mood-associated behaviors without any increase in seizure susceptibility. Focusing on prelimbic layer 5 (L5) pyramidal neurons (PNs) whose activity modulates mood-associated behaviors, we observed changes in neurotransmission and decreased spine density suggestive of L5 PN hypoactivity. ALDH7A1 depletion had a cell-autonomous effect on redox-sensitive calcium signaling in astrocytes but did not induce overt reactivity. Treatment with the indirect antioxidant sulforaphane (SFN), a broccoli-derived phytochemical now commercially-available in concentrated dietary supplements, ameliorated the effect of astrocytic ALDH7A1 deletion on neurotransmission and the mood-associated behavioral deficits that were also found in mice with constitutive global ALDH7A1 depletion. Consistent with these observations, SFN treatment successfully rescued mood-associated behavioral deficits in mice with constitutive global ALDH7A1 depletion; however, SFN treatment did not beneficially affect seizure susceptibility. Together, these findings indicate that ALDH activity in astrocytes is an important redox-associated regulator of cortical circuit function and behavior. These findings suggest that SFN dietary intervention may be an effective treatment for non-ictal symptoms, both in PDE and other conditions with ALDH or redox deficiencies.

Results

Astrocyte ALDH7A1 contributes to non-ictal behavior but not seizure susceptibility

In order to understand the neurobiology of ALDH7A1 dysfunction and the human condition of PDE, we generated *Aldh7a1* floxed mice (*Aldh7a1^{flox/flox}*) (**Fig. 1A**) in which Cre-mediated deletion of exons

4-5 results in loss of ALDH7A1 protein. We crossed *Aldh7a1^flox/flox* mice with the *CMV-Cre* line and interbred the offspring to obtain cre-negative *Aldh7a1^-/-* (ALDH7A1 KO^Global^) mice with constitutive global deletion of *Aldh7a1* in all tissues, modeling the genetic condition of PDE. We validated the deletion of *Aldh7a1* in ALDH7A1 KO^Global^ mice by polymerase chain reaction (PCR) (**Fig. S1A**) and loss of ALDH7A1 protein expression by immunohistochemistry (**Fig. 1B**) and Western blotting (**Fig. 1C**). ALDH7A1 KO^Global^ mice are viable, exhibit no differences in weight (**Fig. S1B**) or locomotion (**Fig. S1C**), and maintain a normal lifespan at least into adulthood. However, ALDH7A1 KO^Global^ mice have increased sensitivity to the chemoconvulsant pentylenetetrazol (PTZ) ($P = 0.0008$, **Fig. 1D**), mimicking the epileptic phenotype observed in PDE. In addition, ALDH7A1 KO^Global^ mice displayed changes in forced swim response (**Fig. 1E**). Thus, ALDH7A1 KO^Global^ mice can serve as a model for both the ictal and non-ictal aspects of PDE.

Following baseline behavioral characterization of ALDH7A1 KO^Global^ mice, we sought to determine the cell type responsible for these behavioral changes. At a tissue level, ALDH7A1 is most abundant in the liver, kidneys, and the brain[27]. In the embryonic brain, ALDH7A1 is expressed by radial glia[28] and postnatally, unbiased mRNA expression analyses indicate that *Aldh7a1* mRNA is highly enriched in astrocytes compared to other cell types in the brain[21,29]. Indeed, we observed ALDH7A1 immunoreactivity in 100% of astrocytes (**Fig. 1F-G**), but only 1% of oligodendrocytes, and not in any microglia, neurons, or Ng2^+ cells in the postnatal brain (**Fig. S2A-D**). This expression pattern held true for all regions sampled (**Fig. S2E-H**). At a total protein level, no differences were observed between male and female mice (**Fig. S2I-J**). However, consistent with transcriptomic data from isolated human astrocytes[21], we observed a developmental increase in ALDH7A1 protein levels from 3 weeks of age to 10 weeks in cortical tissue (**Fig. 1H-I**). These data indicate that ALDH7A1 is predominantly

6

expressed by astrocytes in the postnatal brain and suggest that its astrocytic function is a common feature of mature astrocytes.

Since astrocytes are the primary cellular source of ALDH7A1 within the postnatal brain, we hypothesized that depletion of ALDH7A1 from postnatal astrocytes would be sufficient to induce the behavioral phenotypes observed in ALDH7A1 KO^{Global} mice. We generated mice with conditional deletion of ALDH7A1 in postnatal astrocytes (ALDH7A1 cKO^{Astro} mice) by crossing *Aldh7a1 $^{flox/flox}$* mice to *GLAST-CreER* (*knock-in*) mice and administering 4-hydroxytamoxifen (4-OHT) at P3 and P4. 4-OHT injected, Cre-negative littermates were used as controls. Using this paradigm, ALDH7A1 was depleted from ~90% of cortical astrocytes (**Fig. S1D**) and total protein levels were depleted by ~90% in the cortex and 50% in the rest of the brain (**Fig. S1E**). Paradoxically, ALDH7A1 cKO^{Astro} mice displayed a significantly higher seizure threshold than controls (**Fig 1J**), a relative change in the opposite direction as that observed in ALDH7A1 KO^{Global} mice. These results suggest that, despite its prominent astrocytic expression, ALDH7A1 function in postnatal astrocytes is not the primary driver of the increased sensitivity to chemoconvulsants observed in ALDH7A1 KO^{Global} mice. ALDH7A1 cKO^{Astro} mice did show reduced forced swim test mobility ($t = 2.403$, $P = 0.0371$, **Fig. 1K**), a result that phenocopies the behavior of ALDH7A1 KO^{Global} mice and suggests that ALDH7A1 function in postnatal astrocytes may underlie the deficit in forced swim behavior in both models. These data collectively indicate that PDE may be a condition of pleiotropy in which ALDH7A1 dysfunction in postnatal astrocytes underlies a subset of phenotypes more closely associated with non-ictal symptoms than seizures.

Astrocyte ALDH7A1 influences neuronal excitatory/inhibitory inputs

Previous studies have shown that forced swim mobility is reversibly controlled by the activity of L5 PNs in prelimbic cortex[30]. To broadly determine if neurotransmission is altered in adult ALDH7A1 cKO^{Astro} mice, we recorded miniature excitatory and inhibitory postsynaptic currents (mEPSCs and mIPSCs) from L5 PNs in prelimbic cortex (**Fig. 2A-J**). L5 PNs from ALDH7A1 cKO^{Astro} mice exhibited a significant decrease in the frequency of mEPSCs (t_{27} = 2.07, P = 0.0482, **Fig. 2C**) accompanied by an increase in the frequency of mIPSCs (t_{21} = 2.477, P = 0.0217, **Fig. 2E**). However, spontaneous EPSCs and IPSCs were unaffected by ALDH7A1 depletion (**Fig. S3A-D**), suggesting that the changes in mEPSC and mIPSC frequencies are due to changes in synapse numbers on L5 PNs. There was also no change in the amplitude of mEPSCs or mIPSCs (**Fig. 2D**, **F**), indicating that postsynaptic receptor densities at these synapses were unaltered. Thus, ALDH7A1 depletion from postnatal astrocytes reduces excitatory synapses and increases inhibitory synapses on L5 PNs, leading to E-I imbalance characterized by hypo-excitation of L5 PNs. These changes in excitatory/inhibitory inputs are consistent with the behavioral changes in ALDH7A1 cKO^{Astro} mice and suggest that the reduced forced swim test mobility may be a result of hypo-active L5 PNs.

Astrocyte ALDH7A1 depletion selectively reduces dendritic spine density in layer 5

To confirm whether astrocyte ALDH7A1 influences excitatory synapse density on L5 PNs in adult ALDH7A1 cKO^{Astro} mice, we examined the distribution of dendritic spines on L5 PNs (**Fig. 3A, B**). We analyzed spine density on primary apical, secondary apical, and basal dendrites separately and included layer 2/3 (L2/3) PNs in our analysis to determine whether the effect of ALDH7A1 deletion is specific to L5 PNs. Intriguingly, spine density was decreased in ALDH7A1 cKO^{Astro} mice (**Fig. 3C**), but not universally across all synapses. Astrocytic ALDH7A1 depletion had a significant effect on the basal dendrites of L5 PNs (t_{26} = 2.887, P = 0.0455), but not on L5 PN primary or secondary apical dendrites (**Fig. 3C**). Astrocytic ALDH7A1 depletion also did not affect spine density on L2/3 PNs

(**Fig. 3C**). These results suggest that astrocytic ALDH7A1 depletion only affects spine density at specific locations, either due to differences in the postsynaptic neurons, their inputs, or the astrocytes that contact each individual spine. Further analysis of dendritic spine density along L5 PN primary apical dendrites revealed a reduction in apical dendrite spine density on the portion contained within L5 (t_{47} = 2.646, P = 0.0328, **Fig. 3D**). In conjunction with the reduction in spine density on basal dendrites which are primarily located in L5, these data strongly suggest that the heterogeneous effect of ALDH7A1 depletion on spine density is due to differences in astrocyte-spine interactions specific to L5.

We also examined the density of inhibitory synapses in ALDH7A1 cKO^{Astro} mice. However, since inhibitory synapses do not form on spines, they cannot be detected by Golgi-Cox staining. Instead, we used immunofluorescence to assess colocalization of pre- and post-synaptic proteins, VGAT and gephyrin, at inhibitory synapses in ALDH7A1 cKO^{Astro} mice (**Fig. S3E**). The density of inhibitory synaptic puncta in L2/3 and L5 of ALDH7A1 cKO^{Astro} mice did not significantly differ from controls ($F_{1,16}$ = 0.2518, P = 0.5805, **Fig. S3F**), suggesting that astrocytic ALDH7A1 depletion does not induce a global increase in the density of inhibitory synaptic puncta. However, because all inhibitory synapses were included in this analysis, not just those onto L5 PNs, we cannot exclude the possibility that ALDH7A1 depletion selectively increases inhibitory synapse density on L5 PNs.

ALDH7A1 regulates redox-sensitive microdomain Ca^{2+} signaling in astrocytes
The changes in excitatory/inhibitory inputs on L5 PNs suggest that loss of ALDH7A1 in astrocytes may disrupt astrocyte-neuron interactions in prelimbic cortex involved in synapse formation/elimination. There are several mechanisms by which astrocytes can influence spine number on neurons[31], but it is unclear how a house-keeping enzyme such as an ALDH7A1 might influence

9

these processes. Based on the function of ALDH7A1 in peripheral cells in redox homeostasis[32], we hypothesized that ALDH7A1 depletion in astrocytes could affect synapse formation/elimination by inducing oxidative stress in astrocytes and/or by disrupting astrocytic functions that depend on proper redox signaling. To examine ALDH7A1 function at a cell autonomous level while preserving *in vivo* astrocyte-neuron interactions, we pursued a mosaic deletion strategy[33] in which we could compare intermixed ALDH7A1[+] and ALDH7A1^{−} cells from within the same animal. We therefore generated *Aldh7a1[flox/flox]; BAC-GLAST-CreER[+]; R26-LSL-mGCaMP3[flox/+]* mice (ALDH7A1 cKO[Astro(Mosaic)]) and injected 4-OHT at P3 and P4 to induce ALDH7A1 depletion in ~50% of cortical astrocytes and sparse labeling of ALDH7A1[+] and ALDH7A1[−] astrocytes with membrane-bound GCaMP3 (**Fig. 4A, B, S5A**). Using ALDH7A1 cKO[Astro(Mosaic)] mice, we were able to assess the effect of ALDH7A1 depletion on astrocytic morphology and intracellular Ca^{2+} signaling at a cell autonomous level.

Astrocyte morphology affects synaptogenesis[34] and astrocytic neurotransmitter uptake[35] and is modulated by redox regulation of cytoskeletal dynamics[36], cell growth[37], and the induction of reactive gliosis[38] which is characterized in part by increased cell size. However, in ALDH7A1 cKO[Astro(Mosaic)] mice, we did not observe differences in the "territory volume"[34] of ALDH7A1^{−} cells compared to ALDH7A1^{+} cells, suggesting that ALDH7A1 function does not significantly affect astrocyte distribution ($t_{21} = 0.5520$, $P = 0.5867$, **Fig. S4A, B**) or induce hypertrophic astrocyte reactivity. Furthermore, ALDH7A1[−] astrocytes did not demonstrate the gliotic GFAP staining characteristic of reactive astrocytes (**Fig. S5B**), suggesting that ALDH7A1[−] astrocytes are not classically defined "reactive astrocytes". ALDH7A1[−] astrocytes did show a significant increase in the "neuropil infiltration volume" (NIV)[34] ($F_{1,59} = 8.369$, $P = 0.0053$, **Fig. S4C, D**), a measure of the volume of astrocytic processes in synaptic regions, but this increase in astrocyte NIV was only observed in L2/3 ($t_{59} = 2.38$, $P = 0.0411$), not in L5 ($t_{59} = 1.659$, $P = 0.2048$). Thus, although ALDH7A1 depletion

10

causes morphological changes in a subset of astrocytes, the spatial distribution of these morphological changes (in L2/3) does not overlap with the decrease in PN spine density (in L5) and is therefore unlikely to underlie the synaptic changes we observed in ALDH7A1 cKO^{Astro} mice.

In addition to morphological changes, we assessed if ALDH7A1 depletion affects astrocyte microdomain Ca^{2+} signaling in acute cortical brain slices (**Fig. 4C-I**). Astrocyte Ca^{2+} signals in the fine cell processes or "microdomains" respond to local synaptic events[39] and are particularly sensitive to ROS[40]. Genetically-encoded fluorescence Ca^{2+} indicators provide us a real-time readout of a redox-dependent process in astrocytes. At baseline, neither the frequency nor amplitude of Ca^{2+} transients (**Fig. 4G, H**), nor the number of active microdomains (**Fig. 4I**) were different between ALDH7A1^{+} and ALDH7A1^{-} cells, suggesting that ALDH7A1^{-} cells do not have altered Ca^{2+} signaling or elevated levels of ROS at baseline. This result was further supported by immunohistochemical analysis of the oxidative stress marker 8-oxo-dG in ALDH7A1 cKO$^{Astro(Mosaic)}$ tissue (**Fig. S5C**). However, following acute exposure to tert-butyl hydrogen peroxide (tBHP), a compound that increases ROS production[41], the frequency of Ca^{2+} transients was significantly higher in ALDH7A1^{-} cells than ALDH7A1^{+} cells (t_{34} = 2.513, P = 0.0429, **Fig. 4G**). Event amplitudes (**Fig. 4H**) and the number of active domains (**Fig. 4I**) were similar between ALDH7A1^{-} and ALDH7A1^{+} astrocytes. These results suggest that ALDH7A1 depletion in astrocytes increases sensitivity to ROS and enhances local Ca^{2+} signaling in their processes during acute ROS elevations, potentially dysregulating redox-sensitive signaling events that occur in astrocytic processes near synapses.

SFN ameliorates astrocyte ALDH7A1-induced excitatory-inhibitory imbalance

Our results suggest that ALDH7A1 depletion affects redox-dependent astrocytic functions that affect L5 PN spine density and excitatory-inhibitory inputs. We therefore hypothesized that activation of

11

ALDH isoenzymes and other antioxidant systems in astrocytes could rescue the effect of ALDH7A1 depletion on L5 PNs in ALDH7A1 cKO[Astro] mice. Whereas direct antioxidants such as vitamin C are short-lived and may elicit pro-oxidant effects, indirect antioxidants such as SFN activate the NF-E2-related factor 2 (Nrf2) pathway to induce expression of cytoprotective, catalytic enzymes including ALDH isoenzymes[42]. In addition, SFN directly binds with some ALDH isoenzymes and increases their enzymatic activity[43]. Accordingly, SFN-induced upregulation of ALDH isoenzymes has been shown to compensate for loss of ALDH activity in ethanol metabolism[44]. SFN remains stable and bioactive in rodent chow (**Fig. S6A**), and oral administration is sufficient to increase levels of glutathione[45], allowing for long-term dietary supplementation. Dietary SFN supplementation has therapeutic relevance as it is safely tolerated in humans and under investigation for the treatment of a variety of disorders in humans[46-49]. We therefore developed a therapeutic strategy to deliver SFN to ALDH7A1 cKO[Astro] mice from 3 weeks of age until adulthood. This SFN diet was safely tolerated and did not affect animal bodyweight (**Fig. S6B**). To determine the impact of the SFN diet on astrocytic ALDH7A1, we directly compared SFN-treated ALDH7A1 cKO[Astro] mice and SFN-treated controls. In doing so, we controlled for the effects of SFN that are independent of astrocytic ALDH7A1, which should be consistent between ALDH7A1 cKO[Astro] mice and control mice. Thus, by dietary administration of SFN, we could test whether activation of ALDH isoenzymes and other antioxidant systems in astrocytes rescues the effects of astrocytic ALDH7A1 depletion.

We first measured the impact of the SFN diet on dendritic spine density in ALDH7A1 cKO[Astro] mice. In mice treated with the SFN diet, we observed no difference between ALDH7A1 cKO[Astro] mice and controls in dendritic spine density on primary apical or basal dendrites (**Fig. 5A**). Furthermore, in comparing SFN-treated ALDH7A1 cKO[Astro] mice and SFN-treated controls, we did not observe any difference in spine density on the portion of the primary apical dendrite in layer 5 (**Fig. 5B**). In

12

comparison with our data on the effect of ALDH7A1 depletion on dendritic spine density in untreated ALDH7A1 cKO^Astro mice, these data suggest that SFN treatment diminishes the effect of astrocytic ALDH7A1 depletion on L5 PN dendritic spine density, thereby rescuing the astrocytic ALDH7A1 deficiency (**Fig. 5C-D**). We then analyzed the effects of SFN treatment on mEPSCs and mIPSCs recorded from L5 PNs. In comparing SFN-treated ALDH7A1 cKO mice and SFN-treated controls, we observed no significant difference in the frequency or amplitude of mEPSCs or mIPSCs (**Fig. 5E-N**), suggesting that SFN-treatment rescues the effect of ALDH7A1 depletion on mEPSC and mIPSC frequency (**Fig. 5O-R**). Together, these results imply that astrocyte redox imbalance underlies changes in spine density and neurotransmission observed in ALDH7A1 cKO^Astro mice. Furthermore, these data suggest that SFN dietary intervention may be an effective therapeutic strategy against astrocytic ALDH7A1 depletion.

SFN ameliorates non-ictal behavior, but not seizure susceptibility, in ALDH7A1 knockout mice

Since SFN dietary intervention rescued the effect of astrocytic ALDH7A1 depletion on L5 PN synaptic inputs, we also expected that SFN treatment would rescue the deficits in forced swim test mobility, a behavior associated with L5 PN activity in prelimbic cortex. In ALDH7A1 cKO^Astro mice treated with SFN, we observed no difference in forced swim test mobility compared to SFN-treated controls (**Fig. 6A**). SFN also reduced the paradoxically increased resilience to PTZ-induced seizures in ALDH7A1 cKO^Astro mice compared to SFN-treated controls (**Fig. 6B**), further implying that SFN treatment rescues E-I imbalance in ALDH7A1 cKO^Astro mice (**Fig. 6C-D**). These behavioral results are consistent with our data showing that SFN dietary treatment rescues the reduced L5 PN spine density, reduced mEPSC frequency, and increased mIPSC frequency caused by astrocytic ALDH7A1 depletion.

We then hypothesized that astrocytic ALDH7A1 depletion might be the primary driver of forced swim test deficits in ALDH7A1 KO^{Global} mice and that the forced swim mobility of these mice might also respond to dietary SFN treatments. Indeed, following SFN dietary treatment, ALDH7A1 KO^{Global} mice had no difference in forced swim test behavior compared to SFN-treated controls (**Fig. 6E**). However, SFN-treated ALDH7A1 KO^{Global} mice still had a significantly increased seizure response to PTZ (**Fig. 6F**), suggesting that SFN cannot rescue the effect of constitutive global ALDH7A1 depletion on seizure activity (**Fig. 6G-H**). These results are consistent with the observation that selective depletion of ALDH7A1 in astrocytes does not increase seizure susceptibility, but instead increases seizure resilience. Thus, in the context of constitutive global ALDH7A1 depletion, SFN is effective in treating non-ictal phenotypes associated with astrocytic redox imbalance caused by ALDH7A1 depletion in astrocytes, but not seizure susceptibility.

Discussion

The present study demonstrates the impact of astrocytic ALDH7A1 on prefrontal E-I balance and identifies SFN as an effective intervention against the astrocyte-associated ALDH dysfunction. Constitutive global deletion of *A1dh7a1* models both ictal and non-ictal symptoms in PDE patients with ALDH7A1 dysfunction, yet selective depletion of ALDH7A1 in astrocytes only replicated the prefrontally-mediated mood-associated behavior changes, not the increased seizure susceptibility. Investigation of the prefrontal circuitry regulating mood-associated behavior revealed that selective depletion of ALDH7A1 in astrocytes produced changes in the frequency of miniature synaptic events and layer-specific differences in dendritic spine density. Using a mosaic deletion model, we found that ALDH7A1 loss of function in astrocytes cell autonomously disrupts astrocyte morphology and redox-mediated Ca^{2+} signals within astrocytes. We therefore developed a diet containing the antioxidant SFN to target ALDH deficiency and redox dysregulation in astrocytes. SFN dietary intervention rescued the

effect of astrocytic ALDH7A1 depletion on dendritic spine density and the frequency of miniature synaptic events, suggesting that astrocytic redox dysregulation underlies these changes. SFN diet also rescued the effect of ALDH7A1 depletion on mood-associated behavior in both mice with astrocyte-specific ALDH7A1 depletion and mice with constitutive global ALDH7A1 depletion, but not seizure threshold deficits in mice with constitutive global ALDH7A1 deletion.

This study focused primarily on the contribution of astrocyte ALDH7A1 depletion to cortical excitatory-inhibitory imbalance and mood alteration, but it is still unclear why constitutive global ALDH7A1 deletion causes increased seizure susceptibility. Since ALDH7A1 is primarily expressed in astrocytes within the postnatal brain, we had expected to observe a similar seizure phenotype in mice with constitutive global ALDH7A1 depletion and mice with astrocyte-specific depletion of ALDH7A1. However, the results of our study suggest that PDE may represent a pleiotropic condition. Other possible sources of ALDH7A1 which are not affected in ALDH7A1 cKO[Astro] include ependymal cells, choroid plexus cells, prenatal glial populations including radial glia and immature astrocytes[28], and peripheral tissues such as the liver[27]. The *Aldh7a1*[flox/flox] line may be of continued use to investigate ALDH7A1 function in these cell populations and their contribution to seizure susceptibility.

The results here demonstrate that astrocytic ALDH activity and "redox" signaling are key factors in the regulation of astrocyte-neuron interactions. Astrocytic redox state is affected by metabolic interactions between astrocytes and neurons during neuronal activity and could potentially serve as a major mediator of astrocyte-neuron interactions[50], allowing astrocytes to actively modify their physiology in response to neuronal cues dependent on their own redox state. Here, we show that astrocyte-originated redox imbalance can cause cortical E-I imbalance and behavioral changes associated with changes in dendritic spine density and neurotransmission at synapses onto L5 PNs. These neuronal changes may

15

be due to ALDH7A1 depletion on astrocyte morphology or astrocyte redox-dependent microdomain Ca^{2+} signaling. Follow-up studies are needed to determine why L5 PNs are preferentially affected and why excitatory synapses are decreased while inhibitory synapses are increased. The fact that L5 PN spines within L5 are the most severely affected suggests that redox imbalance particularly affects the function of L5 astrocytes. Astrocyte morphology varies between cortical layers[34] and cortical astrocytes exhibit layer-specific expression patterns[51-53], but the functional consequences of such differences on synapse density have not been thoroughly characterized. Two recent studies showed that disruption of potassium channel expression in deep layer astrocytes preferentially affects spine density on L5 PNs[54] and that L5 astrocytes regulate local synapse density through release of norrin[55]. Thus, one intriguing possibility to consider is that redox imbalance could disrupt astrocytic Ca^{2+} signaling regulating the release of synaptogenic molecules. However, given the high expression of ALDHs in astrocytes and their cell-type specific expression pattern, there are likely still many unexplored aspects of astrocyte ALDH biology.

Lastly, these results suggest that an SFN-supplemented diet can selectively treat non-ictal behavioral deficits caused by astrocytic ALDH7A1 dysfunction in mice with constitutive global ALDH7A1 dysfunction. SFN may therefore have therapeutic potential for PDE patients who have loss-of-function mutations in *ALDH7A1*. Although seizures can be prevented by vitamin B6 supplementation, PDE patients still suffer from non-ictal symptoms which do not respond to vitamin B6[56]. Since SFN is a natural and safely tolerated compound in humans, it could be tested as an adjuvant therapy to vitamin B6 for non-ictal symptoms in PDE patients. SFN may also have broader application against ALDH deficiencies and astrocyte redox imbalance in other brain disorders. Mutations, copy number variations, and polymorphisms in other ALDH isoenzymes are known to cause neuropsychiatric symptoms and affect emotional and cognitive symptoms in diseases such as Bipolar disorder and

16

Parkinson's disease[20,57,58]. ALDH deficiency and/or associated aldehyde toxicity could additionally be involved in the disease pathophysiology of diseases with excess oxidative stress such as autism spectrum disorder and schizophrenia[59-61]. These genetic ALDH deficiencies could be treated by using SFN to compensate for the affected ALDH isoenzyme, particularly the cognitive and mood dysfunctions in these diseases that may involve cortical E-I imbalance. Due to its function as an indirect antioxidant, SFN is already under clinical investigation for autism spectrum disorder[46] and has been suggested as a possible therapy for cognitive deficits in schizophrenia[45]. Due to its effect on ALDHs, SFN could be particularly effective in subsets of patients with ALDH deficiency/aldehyde toxicity. In the future, SFN could also be used as a lead compound to help identify additional compounds which target the conserved ALDH catalytic cysteine residue and augment ALDH enzymatic activity, opening the possibility for more refined modification of ALDH activities specific to a given ALDH isoenzyme or a particular aldehyde substrate.

Acknowledgements

Author Contributions

Conceptualization and Methodology, T.E.F. and A.S.; Formal analysis, T.E.F., W.X., A.A., and B.L.; Investigation, T.E.F, W.X., A.A. B.L., T.C.-P., S.S., T.P., D.W., J.W.F., and H. J.-P.; Writing, T.E.F. and A.S; Supervision, D.E.B. and A.B.; Funding acquisition, A.S.

Declaration of Interests

The authors declare no competing interests.

18

References

1   Tellez-Zenteno, J. F., Patten, S. B., Jette, N., Williams, J. & Wiebe, S. Psychiatric comorbidity in epilepsy: a population-based analysis. *Epilepsia* **48**, 2336-2344, doi:10.1111/j.1528-1167.2007.01222.x (2007).

2   Deykin, E. Y. & Macmahon, B. Incidence of Seizures among Children with Autistic Symptoms. *Am J Psychiat* **136**, 1310-1312 (1979).

3   Insel, B. J., Ottman, R. & Heiman, G. A. Mood disorders in familial epilepsy: A test of shared etiology. *Epilepsia* **59**, 431-439, doi:10.1111/epi.13985 (2018).

4   Cascella, N. G., Schretlen, D. J. & Sawa, A. Schizophrenia and epilepsy: is there a shared susceptibility? *Neurosci Res* **63**, 227-235 (2009).

5   Brainstorm, C. *et al.* Analysis of shared heritability in common disorders of the brain. *Science* **360**, doi:10.1126/science.aap8757 (2018).

6   Duman, R. S., Sanacora, G. & Krystal, J. H. Altered Connectivity in Depression: GABA and Glutamate Neurotransmitter Deficits and Reversal by Novel Treatments. *Neuron* **102**, 75-90, doi:10.1016/j.neuron.2019.03.013 (2019).

7   Badawy, R. A., Freestone, D. R., Lai, A. & Cook, M. J. Epilepsy: Ever-changing states of cortical excitability. *Neuroscience* **222**, 89-99, doi:10.1016/j.neuroscience.2012.07.015 (2012).

8   Uhlhaas, P. J. & Singer, W. Abnormal neural oscillations and synchrony in schizophrenia. *Nat Rev Neurosci* **11**, 100-113, doi:10.1038/nrn2774 (2010).

9   Mills, P. B. *et al.* Mutations in antiquitin in individuals with pyridoxine-dependent seizures. *Nat Med* **12**, 307-309, doi:10.1038/nm1366 (2006).

10   Baxter, P., Griffiths, P., Kelly, T. & Gardner-Medwin, D. Pyridoxine-dependent seizures: demographic, clinical, MRI and psychometric features, and effect of dose on intelligence quotient. *Developmental medicine and child neurology* **38**, 998-1006 (1996).

11   Baynes, K., Farias, S. T. & Gospe, S. M., Jr. Pyridoxine-dependent seizures and cognition in adulthood. *Developmental medicine and child neurology* **45**, 782-785 (2003).

12   van Karnebeek, C. D. *et al.* Lysine restricted diet for pyridoxine-dependent epilepsy: first evidence and future trials. *Mol Genet Metab* **107**, 335-344, doi:10.1016/j.ymgme.2012.09.006 (2012).

13   Vasiliou, V. & Nebert, D. W. Analysis and update of the human aldehyde dehydrogenase (ALDH) gene family. *Human genomics* **2**, 138-143 (2005).

14   Wang, M. F., Han, C. L. & Yin, S. J. Substrate specificity of human and yeast aldehyde dehydrogenases. *Chemico-biological interactions* **178**, 36-39, doi:10.1016/j.cbi.2008.10.002 (2009).

15   O'Brien, P. J., Siraki, A. G. & Shangari, N. Aldehyde sources, metabolism, molecular toxicity mechanisms, and possible effects on human health. *Critical reviews in toxicology* **35**, 609-662 (2005).

16   Vasiliou, V., Pappa, A. & Estey, T. Role of human aldehyde dehydrogenases in endobiotic and xenobiotic metabolism. *Drug metabolism reviews* **36**, 279-299, doi:10.1081/DMR-120034001 (2004).

17   LoPachin, R. M. & Gavin, T. Molecular Mechanisms of Aldehyde Toxicity: A Chemical Perspective. *Chem Res Toxicol* **27**, 1081-1091, doi:10.1021/tx5001046 (2014).

18   Nebert, D. W. *et al.* Role of the aromatic hydrocarbon receptor and [Ah] gene battery in the oxidative stress response, cell cycle control, and apoptosis. *Biochemical pharmacology* **59**, 65-85 (2000).

19   Uma, L., Hariharan, J., Sharma, Y. & Balasubramanian, D. Corneal aldehyde dehydrogenase displays antioxidant properties. *Experimental eye research* **63**, 117-120 (1996).

20   Vasiliou, V. & Pappa, A. Polymorphisms of human aldehyde dehydrogenases. Consequences for drug metabolism and disease. *Pharmacology* **61**, 192-198, doi:10.1159/000028400 (2000).

21   Zhang, Y. *et al.* Purification and Characterization of Progenitor and Mature Human Astrocytes Reveals Transcriptional and Functional Differences with Mouse. *Neuron* **89**, 37-53, doi:10.1016/j.neuron.2015.11.013 (2016).

22   Cahoy, J. D. *et al.* A transcriptome database for astrocytes, neurons, and oligodendrocytes: a new resource for understanding brain development and function. *The Journal of neuroscience : the official journal of the Society for Neuroscience* **28**, 264-278, doi:10.1523/JNEUROSCI.4178-07.2008 (2008).

23   Gong, S. *et al.* A gene expression atlas of the central nervous system based on bacterial artificial chromosomes. *Nature* **425**, 917-925, doi:10.1038/nature02033 (2003).

24   Verkhratsky, A., Nedergaard, M. & Hertz, L. Why are astrocytes important? *Neurochemical research* **40**, 389-401, doi:10.1007/s11064-014-1403-2 (2015).

25   Allen, N. J. & Eroglu, C. Cell Biology of Astrocyte-Synapse Interactions. *Neuron* **96**, 697-708, doi:10.1016/j.neuron.2017.09.056 (2017).

26   Pannasch, U. *et al.* Astroglial networks scale synaptic activity and plasticity. *Proc Natl Acad Sci U S A* **108**, 8467-8472, doi:10.1073/pnas.1016650108 (2011).

27   Brocker, C. *et al.* Aldehyde dehydrogenase 7A1 (ALDH7A1) is a novel enzyme involved in cellular defense against hyperosmotic stress. *J Biol Chem* **285**, 18452-18463, doi:10.1074/jbc.M109.077925 (2010).

28   Jansen, L. A. *et al.* Glial localization of antiquitin: implications for pyridoxine-dependent epilepsy. *Ann Neurol* **75**, 22-32, doi:10.1002/ana.24027 (2014).

20

29   Zhang, Y. *et al.* An RNA-sequencing transcriptome and splicing database of glia, neurons, and vascular cells of the cerebral cortex. *The Journal of neuroscience : the official journal of the Society for Neuroscience* **34**, 11929-11947, doi:10.1523/JNEUROSCI.1860-14.2014 (2014).

30   Warden, M. R. *et al.* A prefrontal cortex-brainstem neuronal projection that controls response to behavioural challenge. *Nature* **492**, 428-432, doi:10.1038/nature11617 (2012).

31   Chung, W. S., Allen, N. J. & Eroglu, C. Astrocytes Control Synapse Formation, Function, and Elimination. *Cold Spring Harb Perspect Biol* **7**, a020370, doi:10.1101/cshperspect.a020370 (2015).

32   Brocker, C., Cantore, M., Failli, P. & Vasiliou, V. Aldehyde dehydrogenase 7A1 (ALDH7A1) attenuates reactive aldehyde and oxidative stress induced cytotoxicity. *Chem Biol Interact* **191**, 269-277, doi:10.1016/j.cbi.2011.02.016 (2011).

33   Cox, B. C., Liu, Z., Lagarde, M. M. & Zuo, J. Conditional gene expression in the mouse inner ear using Cre-loxP. *Journal of the Association for Research in Otolaryngology : JARO* **13**, 295-322, doi:10.1007/s10162-012-0324-5 (2012).

34   Stogsdill, J. A. *et al.* Astrocytic neuroligins control astrocyte morphogenesis and synaptogenesis. *Nature* **551**, 192-197, doi:10.1038/nature24638 (2017).

35   Oliet, S. H. R., Piet, R. & Poulain, D. A. Control of glutamate clearance and synaptic efficacy by glial coverage of neurons. *Science* **292**, 923-926, doi:DOI 10.1126/science.1059162 (2001).

36   Hung, R. J., Pak, C. W. & Terman, J. R. Direct redox regulation of F-actin assembly and disassembly by Mical. *Science* **334**, 1710-1713, doi:10.1126/science.1211956 (2011).

37   Kim, J. & Wong, P. K. Y. Oxidative Stress Is Linked to ERK1/2-p16 Signaling-mediated Growth Defect in ATM-deficient Astrocytes. *Journal of Biological Chemistry* **284**, 14396-14404, doi:10.1074/jbc.M808116200 (2009).

38   Swanson, R. A., Ying, W. & Kauppinen, T. M. Astrocyte influences on ischemic neuronal death. *Curr Mol Med* **4**, 193-205, doi:Doi 10.2174/1566524043479185 (2004).

39   Di Castro, M. A. *et al.* Local Ca2+ detection and modulation of synaptic release by astrocytes. *Nature neuroscience* **14**, 1276-1284, doi:10.1038/nn.2929 (2011).

40   Agarwal, A. *et al.* Transient Opening of the Mitochondrial Permeability Transition Pore Induces Microdomain Calcium Transients in Astrocyte Processes. *Neuron* **93**, 587-605 e587, doi:10.1016/j.neuron.2016.12.034 (2017).

41   Nieminen, A. L., Byrne, A. M., Herman, B. & Lemasters, J. J. Mitochondrial permeability transition in hepatocytes induced by t-BuOOH: NAD(P)H and reactive oxygen species. *The American journal of physiology* **272**, C1286-1294, doi:10.1152/ajpcell.1997.272.4.C1286 (1997).

42   Cardozo, L. F. *et al.* Nutritional strategies to modulate inflammation and oxidative stress pathways via activation of the master antioxidant switch Nrf2. *Biochimie* **95**, 1525-1533, doi:10.1016/j.biochi.2013.04.012 (2013).

43   Alam, M. F., Laskar, A. A., Maryam, L. & Younus, H. Activation of Human Salivary Aldehyde Dehydrogenase by Sulforaphane: Mechanism and Significance. *PLoS One* **11**, e0168463, doi:10.1371/journal.pone.0168463 (2016).

44   Ushida, Y. & Talalay, P. Sulforaphane accelerates acetaldehyde metabolism by inducing aldehyde dehydrogenases: relevance to ethanol intolerance. *Alcohol Alcohol* **48**, 526-534, doi:10.1093/alcalc/agt063 (2013).

45   Sedlak, T. W. *et al.* Sulforaphane Augments Glutathione and Influences Brain Metabolites in Human Subjects: A Clinical Pilot Study. *Mol Neuropsychiatry* **3**, 214-222, doi:10.1159/000487639 (2018).

46   Singh, K. *et al.* Sulforaphane treatment of autism spectrum disorder (ASD). *Proc Natl Acad Sci U S A* **111**, 15550-15555, doi:10.1073/pnas.1416940111 (2014).

47   Doss, J. F. *et al.* Phase 1 Study of a Sulforaphane-Containing Broccoli Sprout Homogenate for Sickle Cell Disease. *PloS one* **11**, e0152895, doi:10.1371/journal.pone.0152895 (2016).

48   Shiina, A. *et al.* An Open Study of Sulforaphane-rich Broccoli Sprout Extract in Patients with Schizophrenia. *Clinical psychopharmacology and neuroscience : the official scientific journal of the Korean College of Neuropsychopharmacology* **13**, 62-67, doi:10.9758/cpn.2015.13.1.62 (2015).

49   Alumkal, J. J. *et al.* A phase II study of sulforaphane-rich broccoli sprout extracts in men with recurrent prostate cancer. *Investigational new drugs* **33**, 480-489, doi:10.1007/s10637-014-0189-z (2015).

50   Bolanos, J. P. Bioenergetics and redox adaptations of astrocytes to neuronal activity. *Journal of neurochemistry* **139 Suppl 2**, 115-125, doi:10.1111/jnc.13486 (2016).

51   Zeisel, A. *et al.* Brain structure. Cell types in the mouse cortex and hippocampus revealed by single-cell RNA-seq. *Science* **347**, 1138-1142, doi:10.1126/science.aaa1934 (2015).

52   Moroni, R. F., Inverardi, F., Regondi, M. C., Pennacchio, P. & Frassoni, C. Developmental expression of Kir4.1 in astrocytes and oligodendrocytes of rat somatosensory cortex and hippocampus. *International journal of developmental neuroscience : the official journal of the International Society for Developmental Neuroscience* **47**, 198-205, doi:10.1016/j.ijdevneu.2015.09.004 (2015).

53   Saunders, A. *et al.* Molecular Diversity and Specializations among the Cells of the Adult Mouse Brain. *Cell* **174**, 1015-1030 e1016, doi:10.1016/j.cell.2018.07.028 (2018).

54   Hill, S. A. *et al.* Sonic hedgehog signaling in astrocytes mediates cell type-specific synaptic organization. *Elife* **8**, doi:10.7554/eLife.45545 (2019).

55   Miller, S. J. *et al.* Molecularly defined cortical astroglia subpopulation modulates neurons via secretion of Norrin. *Nat Neurosci* **22**, 741-752, doi:10.1038/s41593-019-0366-7 (2019).

56   Stockler, S. *et al.* Pyridoxine dependent epilepsy and antiquitin deficiency: clinical and molecular characteristics and recommendations for diagnosis, treatment and follow-up. *Mol Genet Metab* **104**, 48-60, doi:10.1016/j.ymgme.2011.05.014 (2011).

57   Lu, R. B. *et al.* The aldehyde dehydrogenase 2 polymorphisms on neuropsychological performance in bipolar II disorder with or without comorbid anxiety disorder. *PLoS One* **13**, e0192229, doi:10.1371/journal.pone.0192229 (2018).

58   Yu, R. L., Tan, C. H., Lu, Y. C. & Wu, R. M. Aldehyde dehydrogenase 2 is associated with cognitive functions in patients with Parkinson's disease. *Sci Rep* **6**, 30424, doi:10.1038/srep30424 (2016).

59   Jurnak, F. The Pivotal Role of Aldehyde Toxicity in Autism Spectrum Disorder: The Therapeutic Potential of Micronutrient Supplementation. *Nutr Metab Insights* **8**, 57-77, doi:10.4137/NMI.S29531 (2015).

60   Trepanier, M. O., Hopperton, K. E., Mizrahi, R., Mechawar, N. & Bazinet, R. P. Postmortem evidence of cerebral inflammation in schizophrenia: a systematic review. *Mol Psychiatry* **21**, 1009-1026, doi:10.1038/mp.2016.90 (2016).

61   Emiliani, F. E., Sedlak, T. W. & Sawa, A. Oxidative stress and schizophrenia: recent breakthroughs from an old story. *Curr Opin Psychiatry* **27**, 185-190, doi:10.1097/YCO.0000000000000054 (2014).

62   Schwenk, F., Baron, U. & Rajewsky, K. A cre-transgenic mouse strain for the ubiquitous deletion of loxP-flanked gene segments including deletion in germ cells. *Nucleic acids research* **23**, 5080-5081 (1995).

63   Paukert, M. *et al.* Norepinephrine controls astroglial responsiveness to local circuit activity. *Neuron* **82**, 1263-1270, doi:10.1016/j.neuron.2014.04.038 (2014).

64   Mori, T. *et al.* Inducible gene deletion in astroglia and radial glia--a valuable tool for functional and lineage analysis. *Glia* **54**, 21-34, doi:10.1002/glia.20350 (2006).

65   Regan, M. R. *et al.* Variations in promoter activity reveal a differential expression and physiology of glutamate transporters by glia in the developing and mature CNS. *The Journal of neuroscience : the official journal of the Society for Neuroscience* **27**, 6607-6619, doi:10.1523/JNEUROSCI.0790-07.2007 (2007).

66   Hayashi-Takagi, A. *et al.* Disrupted-in-Schizophrenia 1 (DISC1) regulates spines of the glutamate synapse via Rac1. *Nature neuroscience* **13**, 327-332, doi:10.1038/nn.2487 (2010).

67   Johnson, A. W. *et al.* Cognitive and motivational deficits together with prefrontal oxidative stress in a mouse model for neuropsychiatric illness. *Proceedings of the National Academy of Sciences of the United States of America* **110**, 12462-12467, doi:10.1073/pnas.1307925110 (2013).

68   Ippolito, D. M. & Eroglu, C. Quantifying synapses: an immunocytochemistry-based assay to quantify synapse number. *Journal of visualized experiments : JoVE*, doi:10.3791/2270 (2010).

23

69   Christopherson, K. S. *et al.* Thrombospondins are astrocyte-secreted proteins that promote CNS synaptogenesis. *Cell* **120**, 421-433, doi:10.1016/j.cell.2004.12.020 (2005).

70   Niwa, M. *et al.* Knockdown of DISC1 by in utero gene transfer disturbs postnatal dopaminergic maturation in the frontal cortex and leads to adult behavioral deficits. *Neuron* **65**, 480-489, doi:10.1016/j.neuron.2010.01.019 (2010).

71   Hikida, T. *et al.* Dominant-negative DISC1 transgenic mice display schizophrenia-associated phenotypes detected by measures translatable to humans. *Proceedings of the National Academy of Sciences of the United States of America* **104**, 14501-14506, doi:10.1073/pnas.0704774104 (2007).

72   Frankel, W. N., Yang, Y., Mahaffey, C. L., Beyer, B. J. & O'Brien, T. P. Szt2, a novel gene for seizure threshold in mice. *Genes, brain, and behavior* **8**, 568-576, doi:10.1111/j.1601-183X.2009.00509.x (2009).

73   Bae, Y. S. *et al.* Down-regulation of RalBP1 expression reduces seizure threshold and synaptic inhibition in mice. *Biochemical and biophysical research communications* **433**, 175-180, doi:10.1016/j.bbrc.2013.02.056 (2013).

74   Zhang, Y. S., Wade, K. L., Prestera, T. & Talalay, P. Quantitative determination of isothiocyanates, dithiocarbamates, carbon disulfide, and related thiocarbonyl compounds by cyclocondensation with 1,2-benzenedithiol. *Anal Biochem* **239**, 160-167, doi:DOI 10.1006/abio.1996.0311 (1996).

75   Ye, L. X. *et al.* Quantitative determination of dithiocarbamates in human plasma, serum, erythrocytes and urine: pharmacokinetics of broccoli sprout isothiocyanates in humans (vol 316, pg 43, 2002). *Clin Chim Acta* **321**, 127-129, doi:Pii S0009-8981(02)00007-4 Doi 10.1016/S0009-8981(02)00007-4 (2002).

Fig. 1. Astrocyte ALDH7A1 contributes to non-ictal behavior but not seizure susceptibility

(A) Schematic of targeting vector for generation of floxed *Aldh7a1* mice and floxed *Aldh7a1* allele before and after Cre recombination.

(B) ALDH7A1 immunofluorescence in ALDH7A1 KO[Global] (-/-) mouse and wild-type littermate (+/+). Scale bar: 50 µm.

(C) Western blot of ALDH7A1 in cortical tissue from ALDH7A1 KO[Global] mice (-/-), heterozygous littermates (+/-), and wild-type littermates (+/+).

(D) Severity of seizure response of ALDH7A1 KO[Global] mice (KO) to repeated doses of pentylenetetrazol (PTZ) during a seizure threshold test. The EC_{50} of the dose-response curve is significantly lower in the KO mice compared to WT littermate controls (n = 8 WT mice, 9 KO mice; $F_{1, 62}$ = 12.57, *P = 0.0008)

(E) Proportion of time swimming by KO and WT mice during the forced swim test. Proportion of time swimming was decreased in KO mice compared to WT littermates (n = 28 mice; t_{54} = 2.253, *P = 0.0283).

(F) Co-immunostaining of ALDH7A1 with (A) astrocyte marker ALDH1L1 (arrowhead), in adult mouse cortex. Scale bar: 50 µm. Boxed insets displayed at higher magnification in right three panels. Inset scale bar: 10 µm

(G) Percentage of astrocytes (Aldh1l1), neurons (NeuN), microglia (Iba1), oligodendrocytes (CC1), and oligodendrocyte precursor cells (NG2) expressing ALDH7A1 in adult mouse cortex. Significantly more astrocytes expressed ALDH7A1 compared to other cell types in the brain (n = 4 mice per group; P < 0.0001, $F_{4,15}$ = 119703, one-way ANOVA with Tukey post hoc test: ***P <0.001).

(H-I) Western blot of ALDH7A1 in homogenized cortical tissue at 3 weeks (3w) and 10 weeks (10w) of age. ALDH7A1 expression is increased at 10w. Astrocytic marker ALDH1L1 is shown for reference. (I) Protein expression normalized to GAPDH for quantification. ALDH7A1 expression is

25

significantly higher at 10 weeks of age (3 weeks, $n = 3$ mice; 10 weeks, $n = 4$ mice; 2-way ANOVA with Sidak post hoc test: ALDH7A1: *$P = 0.0249$, ALDH1L1: $P = 0.6067$).

(J) Severity of seizure response of ALDH7A1 cKO^{Astro} mice (cKO) to repeated doses of PTZ during a seizure threshold test. The EC$_{50}$ of the dose-response curve is significantly higher in the cKO mice compared to littermate controls (Con) ($n = 8$ mice per genotype; $F_{1, 58} = 4.970$, *$P = 0.0297$)

(K) Proportion of time swimming by cKO and Con mice during the forced swim test. Proportion of time swimming was decreased in cKO mice (n = 25 cKO, 10 Con mice; $t_{33} = 2.354$, *$P = 0.0247$).

Data in (D), (E), (G), (I), (J), and (K) are represented as mean $\pm$ S.E.M.

Fig. 2. Astrocyte ALDH7A1 influences neuronal excitatory/inhibitory inputs

(A-B) Representative traces of (A) miniature excitatory postsynaptic currents (mEPSCs) and (B) miniature inhibitory postsynaptic currents (mIPSCs) in layer 5 (L5) pyramidal neurons of ALDH7A1 cKO^{Astro} (cKO) mice and controls (Con).

(C) Quantification of mEPSC frequency in L5 pyramidal neurons in cKO and control mice. mEPSC frequency was significantly decreased in cKO mice compared to controls (Con, n = 16 cells; cKO, n = 13 cells; *P = 0.0482, t_{27} = 2.07, two-sided Welch's t-test).

(D) Quantification of mEPSC amplitude in L5 pyramidal neurons in cKO and control mice. No differences were observed (Con, n = 16 cells; cKO, n = 13 cells; P = 0.1028, t_{23} = 1.698, two-sided Welch's t-test).

(E) Quantification of mIPSC frequency in L5 pyramidal neurons in cKO and control mice. mIPSC frequency was significantly increased in cKO mice compared to controls (Con, n = 17 cells; cKO, n = 16 cells; *P = 0.0217, t_{21} = 2.477, two-sided Welch's t-test).

(F) Quantification of mIPSC amplitude in L5 pyramidal neurons in cKO and control mice. No differences were observed (Con, n = 17 cells; cKO, n = 16 cells; P = 0.7406, t_{30} = 0.334, two-sided Welch's t-test).

(G) Cumulative frequency plot of mEPSC inter-event intervals in L5 pyramidal neurons in cKO and control mice (Con, n = 4089 events; cKO, n = 3617 events; P <0.0001, D = 0.101, two-sided Kolmogorov-Smirnov test).

(H) Cumulative frequency plot of mEPSC amplitudes in L5 pyramidal neurons in cKO and control mice (Con, n = 4120 events; cKO, n = 3658 events; P <0.0001, D = 0.149, two-sided Kolmogorov-Smirnov test).

27

(I) Cumulative frequency plot of mIPSC inter-event intervals in L5 pyramidal neurons in cKO and control mice (Con, $n = 6653$ events; cKO, $n = 5220$ events; $P < 0.0001$, $D = 0.111$, two-sided Kolmogorov-Smirnov test)

(J) Cumulative frequency plot mIPSC amplitudes in L5 pyramidal neurons in cKO and control mice (Con, $n = 6688$ events; cKO, $n = 5257$ events; $P = 0.146$, $D = 0.021$, two-sided Kolmogorov-Smirnov test).

Data in (C-F) are represented as mean $\pm$ S.E.M.

Fig. 3. Astrocyte ALDH7A1 depletion selectively reduces dendritic spine density in layer 5

(A) Schematic of layer 2/3 (L2/3) and layer 5 (L5) pyramidal neuron (PNs) in prelimbic cortex and the relative position of primary (1^{ry}) apical, secondary (2^{ry}) apical, and basal dendrites within the cortical layers.

(B) Representative Golgi-Cox stained basal dendrites of L5 PNs in prelimbic cortex of ALDH7A1 cKO^{Astro} (cKO) and control (Con) mice. Dendritic spines in left image are pseudocolored yellow in right duplicate image. Scale bar: 10 µm.

(C) Spine density on the 1^{ry} apical, 2^{ry} apical, and basal dendrites of L2/3 PNs and L5 PNs of cKO and Con mice. Spine density is significantly decreased on L5 PNs in cKO mice compared to Con, but not on L2/3 PNs; the spine density on L5 PNs is significantly decreased on basal dendrites in cKO mice, but not 1^{ry} or 2^{ry} dendrites (L2/3:Con:1^{ry} Apical, n = 12 cells; L2/3:Con:2^{ry} Apical, n = 12 cells; L2/3:Con:Basal, n = 12 cells; L2/3:cKO:1^{ry} Apical, n = 16 cells; L2/3:cKO:2^{ry} Apical, n = 13 cells; L2/3:cKO:Basal, n = 15 cells; L5:Con:1^{ry} Apical, n = 11 cells; L5:Con:2^{ry} Apical, n = 10 cells; L5:Con:Basal, n = 12 cells; L5:cKO:1^{ry} Apical, n = 16 cells; L5:cKO:2^{ry} Apical, n = 15 cells; L5:cKO:Basal, n = 16 cells; Genotype: P = 0.2594, $F_{1,148}$ = 1.282; Cell body layer: P = 0.00004, $F_{1,148}$ = 17.78; Dendrite subtype: P = 0.0529, $F_{2,148}$ = 1.998; Genotype:Cell body layer: P = 0.0013, $F_{1,148}$ = 10.72; Genotype:Dendrite subtype P = 0.8919, $F_{2,148}$ = 0.115; Cell body layer:Dendrite subtype: P = 0.0021, $F_{2,148}$ = 6.442; Genotype:Cell body layer:Dendrite subtype: P = 0.911, $F_{2,148}$ = 0.094; 3-way ANOVA of linear model, Holm-Sidak post hoc test of selected pairs: L2/3 PN 1^{ry} apical, P = 0.7569, t_{26} = 0.8914; L2/3 PN 2^{ry} apical, P = 0.7569, t_{23} = 0.9031; L2/3 PN basal, P = 0.7569, t_{25} = 0.7095; L5 PN 1^{ry} apical, P = 0.2073, t_{25} = 2.106; L5 PN 2^{ry} apical, P = 0.5580, t_{23} = 1.368; L5 PN basal, *P = 0.0455, t_{26} = 2.887).

(D) Spine density on 1^{ry} apical dendrites of L5 PNs in cKO and Con mice binned by cortical layer. Spine density on L5 PN 1^{ry} apical dendrites is decreased in cKO mice within cortical layer L5, but not

L2/3 or layer 1 (L1) (Con:L1, n = 3 cells; Con:L2/3, n = 10 cells; Con:L5, n = 8 cells; cKO:L1, n = 5 cells; cKO:L2/3, n = 15 cells; cKO:L5, n = 12 cells; Genotype: P = 0.0446, $F_{1,47}$ = 4.598; Spine layer: P = 0.0273, $F_{2,47}$ = 4.055; Interaction: P = 0.2778, $F_{2,47}$ = 1.335; 2-way ANOVA of mixed linear model, Holm-Sidak post hoc test of selected pairs: L1, P = 0.9997; t_{47} = 0.0823; L2/3, P = 0.7477, t_{47} = 0.9807 ; L5, *P = 0.0328, t_{47} = 2.646).

Data in (C-D) are represented as mean $\pm$ S.E.M.

30

Fig. 4. ALDH7A1 regulates redox-sensitive microdomain Ca²⁺ signaling in astrocytes

(A-B). ALDH7A1 immunofluorescence in ALDH7A1 cKO$^{Astro(Mosaic)}$ mice (scale bars: 200 µm in A, 20 µm in B). ALDH7A1+ (arrowhead) and ALDH7A1⁻ (arrow) astrocytes expressing mGCaMP3 are indicated.

(C) Median intensity projection image (pseudocolored) of 540 frames of one ALDH7A1⁺ astrocyte (outlined; left) and one ALDH7A1⁻ astrocyte (right) after incubation with tert-butyl hydrogen peroxide (tBHP). Scale bar, 10 µm.

(D) Map of microdomains recorded in one ALDH7A1⁺ astrocyte (left) and one ALDH7A1⁻ (right) after tBHP incubation. Outlines indicate cell border. Scale bar, 10 µm.

(E) Intensity vs. time traces for 5 microdomains (corresponding to colors in D) depicting Ca²⁺ transients in ALDH7A1⁺ and ALDH7A1⁻ astrocytes after tBHP incubation.

(F) Raster plots showing timing and intensity of Ca²⁺ transients in individual microdomains (mD) in ALDH7A1⁺ (left) and ALDH7A1⁻ (right) astrocytes after tBHP incubation.

(G) Quantification of the frequency of microdomain Ca²⁺ transients in ALDH7A1⁺ and ALDH7A1⁻ astrocytes at baseline and after tBHP incubation. After tBHP incubation, the frequency of microdomain Ca²⁺ transients was significantly higher in ALDH7A1⁻ astrocytes compared to ALDH7A1⁺ astrocytes, but not at baseline (ALDH7A1⁺, $n = 10$ cells; ALDH7A1⁻, $n = 9$ cells; Genotype: $P = 0.1509$, $F_{1,17} = 2.263$; Treatment: $P = 0.0095$, $F_{1,17} = 8.527$; Interaction: $P = 0.0429$, $F_{1,17} = 4.790$; Individuals: $P = 0.01163$, $F_{17,17} = 1.807$; two-way repeated measures ANOVA, Bonferroni post hoc test: Baseline: $P = 0.9938$, $t_{34} = 0.0993$; tBHP: *$P = 0.0334$, $t_{34} = 2.513$).

(H) Quantification of Ca²⁺ transient amplitudes in ALDH7A1⁺ and ALDH7A1⁻ astrocytes at baseline and after tBHP incubation. No differences in amplitude were observed (ALDH7A1⁺, $n = 10$ cells; ALDH7A1⁻, $n = 9$ cells; Genotype: $P = 0.3072$, $F_{1,17} = 1.108$; Treatment: $P = 0.1947$, $F_{1,17} = 1.823$; Interaction: $P = 0.8428$, $F_{1,17} = 4.0406$; Individuals: $P = 0.4488$, $F_{17,17} = 1.065$; two-way repeated

31

measures ANOVA, Bonferroni post hoc test: Baseline: $P > 0.99$, $t_{34} = 0.6160$; tBHP; $P = 0.7528$, $t_{34} = 0.8963$).

(I) Number of active microdomains in ALDH7A1$^+$ and ALDH7A1$^-$ astrocytes at baseline and after tBHP incubation. The number of active microdomains was increased after tBHP incubation, but no differences were observed between ALDH7A1$^+$ and ALDH7A1$^-$ astrocytes (ALDH7A1$^+$, $n = 10$ cells; ALDH7A1$^-$, $n = 9$ cells; Genotype: $P = 0.3395$, $F_{1,17} = 0.9659$; Treatment: $P = 0.0006$, $F_{1,17} = 17.67$; Interaction: $P = 0.9152$, $F_{1,17} = 0.0117$; Individuals: $P = 0.0255$, $F_{17,17} = 2.662$; two-way repeated measures ANOVA, Bonferroni post hoc test: Baseline: $P = 0.7548$, $t_{34} = 0.8944$; tBHP: $P = 0.8799$, $t_{34} = 0.7815$).

Data in (G-I) represented as mean $\pm$ S.E.M.

Fig. 5. SFN ameliorates astrocyte ALDH7A1-induced excitatory-inhibitory imbalance.

(A) Spine density on the 1^{ry} apical (Api) and basal dendrites of layer 5 (L5) pyramidal neurons (PN) of ALDH7A1 cKO^{Astro} (cKO) and control (Con) mice treated with SFN diet. No differences were unobserved (Basal dendrites: $n = 12$ Con + SFN, 14 cKO + SFN; 1^{ry} Apical: $n = 12$ Con + SFN, 20 cKO + SFN; two-way ANOVA with Sidak post-hoc test: basal dendrites: $t_{54} = 0.4221$, $P=0.8941$; 1^{ry} apical: $t_{54} = 1.135$, $P = 0.4537$).

(B) Spine density on 1^{ry} apical dendrites of L5 PNs in cKO and Con mice on a diet containing SFN binned by cortical layer. No differences were observed (Con+SFN:L1, $n = 6$ cells; Con+SFN:L2/3, $n = 12$ cells; Con+SFN:L5, $n = 12$ cells; cKO+SFN:L1, $n = 8$ cells; cKO+SFN:L2/3, $n = 20$ cells; cKO+SFN:L5, $n = 16$ cells; mixed-effects model with Sidak's post hoc test: L1: $t_{12} = 1.767$, $P = 0.2797$; L2/3: $t_{29} = 0.8808$, $P = 0.7682$; L5: $t_{17} = 17$, $P = 0.7726$)

(C) L5 PN basal dendrite spine densities from Figs. 3C and 5A normalized to respective dietary controls *P <0.05.

(D) L5 PN 1^{ry} apical dendrites spine density within L5 from Figs. 3D and 5B normalized to respective dietary controls *P <0.05.

(E-F) Representative traces of (E) miniature excitatory postsynaptic currents (mEPSCs) and (F) miniature inhibitory postsynaptic currents (mIPSCs) in prelimbic L5 PNs of cKO and Con mice on a diet containing SFN.

(G) Quantification of mEPSC frequency in cKO and Con mice treated with a diet containing SFN. No differences were observed (Con + SFN, $n = 12$ cells; cKO + SFN, $n = 10$ cells; $P = 0.2950$, $t_{16} = 1.084$, two-sided Welch's t-test).

(H) Quantification of mEPSC amplitude in cKO and Con mice treated with a diet containing SFN. No differences were observed (Con + SFN, $n = 12$ cells; cKO + SFN, $n = 10$ cells; $P = 0.5473$, $t_{19} = 0.6127$, two-sided Welch's t-test).

33

(I) Quantification of mIPSC frequency in cKO and Con mice treated with a diet containing SFN. No differences were observed (Con + SFN, n = 13 cells; cKO + SFN, n = 15 cells; P = 0.5593, t_{25} = 0.5918, two-sided Welch's t-test).

(J) Quantification of mIPSC amplitude in cKO and Con mice treated with a diet containing SFN. No differences were observed (Con + SFN, n = 13 cells; cKO + SFN, n = 15 cells; P = 0.9360, t_{25} = 0.0811, two-sided Welch's t-test).

(K) Cumulative frequency plot of mEPSC inter-event intervals in L5 pyramidal neurons in cKO and Con mice treated with a diet containing SFN (Con + SFN, n = 2345 events; cKO + SFN, n = 1698 events; P <0.0001, D = 0.09316, two-sided Kolmogorov-Smirnov test).

(L) Cumulative frequency plot of mEPSC amplitudes in L5 pyramidal neurons in cKO and control mice treated with a diet containing SFN (Con + SFN, n = 2345 events; cKO + SFN, n = 1698 events; P <0.0001, D = 0.08264, two-sided Kolmogorov-Smirnov test).

(M) Cumulative frequency plot of mIPSC inter-event intervals in L5 pyramidal neurons in cKO and control mice treated with a diet containing SFN (Con + SFN, n = 11493 events; cKO + SFN, n = 10949 events; P <0.0001, D = 0.111, two-sided Kolmogorov-Smirnov test)

(N) Cumulative frequency plot mIPSC amplitudes in L5 pyramidal neurons in cKO and control mice treated with a diet containing SFN (Con + SFN, n = 11493 events; cKO + SFN, n = 10949 events; P < 0.0001, D = 0.03969, two-sided Kolmogorov-Smirnov test).

(O) mEPSC frequency data from Figs. 2C and 5G normalized to dietary controls, *P < 0.05.

(P) mEPSC amplitude data from Figs. 2D and 5H normalized to dietary controls.

(Q) mIPSC frequency data from Figs. 2E and 5I normalized to dietary controls, **P < 0.01.

(R) mIPSC amplitude data from Figs. 2F and 5J normalized to dietary controls.

Data in (A-D), (G-J), and (O-R) are represented as mean $\pm$ S.E.M.

34

Fig. 6. SFN ameliorates non-ictal behavior, but not seizure susceptibility, in ALDH7A1 knockout mice.

(A) Proportion of time swimming by ALDH7A1 cKO[Astro] (cKO) and control (Con) mice on a diet containing SFN during the forced swim test. No differences were observed (n = 16 mice; 3, t_{30} = 2.002, P = 0.0545).

(B) Severity of seizure response of cKO and Con mice on a diet containing SFN to repeated doses of pentylenetetrazol (PTZ) during a seizure threshold test. No difference in the EC_{50} of the dose-response curve was observed (n = 5 Con + SFN mice, 8 cKO + SFN mice; $F_{1, 46}$ = 0.0061, P = 0.9378)

(C) Forced swim mobility data from Figs. 1K and 6A normalized to dietary controls, *P < 0.05.

(D) EC_{50} of PTZ dose-response curve from Figs. 1J and 6B normalized to dietary controls, *P < 0.05.

(E) Proportion of time swimming by ALDH7A1 KO[Global] (KO) and wild-type (WT) mice on a diet containing SFN during the forced swim test. No differences were observed (n = 11 WT + SFN, 13 KO + SFN mice; 3, t_{22} = 0.8141, P = 0.4243).

(F) Severity of seizure response of KO and WT mice on a diet containing SFN to repeated doses of PTZ during a seizure threshold test. The EC_{50} of the dose-response curve was significantly lower in KO + SFN mice (n = 11 WT + SFN, 12 KO + SFN mice; $F_{1, 86}$ = 10.75, ***P = 0.0015).

(G) Forced swim mobility data from Figs. 1E and 6E normalized to dietary controls, *P < 0.05.

(H) EC_{50} of PTZ dose-response curve from Figs. 1D and 6F normalized to dietary controls, ***P < 0.005.

All data are represented as mean $\pm$ S.E.M.

STAR Methods

CONTACT FOR REAGENT AND RESOURCE SHARING

Further information and requests for resources and reagents should be directed to and will be fulfilled by the Lead Contact, Akira Sawa (asawa1@jhmi.edu).

EXPERIMENTAL MODEL AND SUBJECT DETAILS

Mice: Unless otherwise specified, experiments were performed in adult mice 10-16 weeks of age. All animals were healthy and were not immune compromised. Expression analyses were performed in C57Bl6/NTac animals. *Aldh7a1*$^{flox/flox}$ mice were generated and maintained on a C57Bl6/NTac background (see Generation of *Aldh7a1* floxed mice section below). All additional transgenic lines were obtained on a C57Bl6 background and crossed with *Aldh7a1*$^{flox/flox}$ mice for at least two generations. Generation and genotyping of Cre driver lines (*CMV-Cre* [62], *BAC-GLAST-CreER* [63], *GLAST-CreER* (*knock-in*) [64]) and reporter lines (*R26-lsl-mGCaMP3* [40], *GLT1-eGFP* [65]) have been previously described. *Aldh7a1*$^{flox/flox}$ mice were crossed with *CMV-Cre* mice and offspring were interbred to obtain *Aldh7a1*$^{-/-}$; *CMV-Cre*$^{-}$ mice (ALDH7A1 cKO^{Global} mice). *Aldh7a1*$^{flox/flox}$ mice were crossed with *BAC-GLAST-CreER* (*knock-in*) mice to generate ALDH7A1 cKO$^{Astro(Mosaic)}$ mice. *Aldh7a1*$^{flox/flox}$ mice were crossed with *GLAST-CreER* (*knock-in*) mice to generate ALDH7A1 cKO^{Astro} mice. Experimental ALDH7A1 cKO$^{Astro(Mosaic)}$ and ALDH7A1 cKO^{Astro} mice were injected with 4-hydroxytamoxifen (see Tamoxifen section below) for induction of the Cre-loxP system from P3-P4 before sexing and genotyping. Genotyping was performed before weaning and reconfirmed post-mortem. Tamoxifen injected Cre-negative ALDH7A1 cKO littermates were used as controls. Both male and female mice were used for experiments using the ALDH7A1 cKO$^{Astro(Mosaic)}$ model for cell-autonomous studies. Male mice were used for experiments using the ALDH7A1 cKO model for circuitry and behavioral studies. Animals were group housed after weaning and maintained on a 12 hour light/dark cycle with food and water provided *ad libitum*. For studies involving the SFN diet (see

36

Sulforaphane diet section below), cages were randomly assigned to receive standard diet or the SFN diet. With the exception of behavioral studies, animals were never involved in previous procedures or studies. For behavioral experiments, animals were sequentially tested on open field test, forced swim test, and the seizure threshold test. All mice were used in accordance with Johns Hopkins University School of Medicine Institutional Animal Care and Use Committee (IACUC) guidelines.

Generation of Aldh7a1 floxed mice: *Aldh7a1* floxed mice containing a *loxP*-flanked allele of *Aldh7a1* were produced by Taconic Biosciences. The targeting strategy was based on the NM_138600.4 transcript. The targeting vector contained loxP sites located in non-conserved regions flanking a ~2 kb genomic region containing exons 4 and 5 of the *Aldh7a1* gene. Positive selection markers flanked by FRT (Neomycin resistence – NeoR) and F3 (Puromycin resistance – PuroR) sites were inserted into intron 3 and 5 respectively. The targeting vector was generated using BAC clones from the C57Bl/6J RPCIB-731 BAC library and transfected into the C57Bl/6J ES cell line. Homologous recombinant clones were isolated by double positive selection. The *Aldh7a1* floxed allele was obtained afterwards by Flp-mediated removal of the selection markers. Cre mediated recombination of the *Aldh7a1* floxed allele results in deletion of exons 4-5 and generates a frameshift from exon 3 to exons 6-11 resulting a premature stop codon in exon 6.

Genotyping of Aldh7a1 floxed mice: Routine genotyping of *Aldh7a1$^{flox/flox}$* and *Aldh7a1$^{-/-}$* mice was performed by polymerase chain reaction using the following primers at a 2:1:1 ratio: 5'-TCATAGCAGAGCACCTGATACC-3', 5'-AAAGGCTTTGCACCACTGTG-3', 5'-CCTATTGTGAGGGACTTTACCC-3'. These primers amplify a 177bp DNA fragment for the wild-type allele, a 396bp fragment for the floxed allele, and a 303bp fragment for the knockout allele. Gels were visualized using Quantity-One software (Bio-Rad).

Tamoxifen injections: Recombinant deletion of floxed alleles was induced by 2 days of subcutaneous injection of 0.2 mg of 4-hydroxytamoxifen (4-OHT; Sigma H7904, St. Louis, MO, USA), once per day

at P3 and P4. 4-OHT was dissolved in ethanol at 20mg/mL by sonication for long term storage at -80°C. On the day of injection, 4-OHT/ethanol solution was added to corn oil (1:5 ratio), vortexed for 4min, and spun on a speed-vac for 30min to evaporate the ethanol before injection.

METHOD DETAILS

Experimental design: Behavioral tests were performed in at least 12 animals per condition for forced swim test and at least 8 animals per condition for open field test and seizure threshold test. Scoring of behavioral tests were performed by experimenters blinded to the experimental conditions. Whole cell recordings and analyses were performed in at least 7 cells from at least 3 animals per condition by experimenters blinded to experimental groups; the order of mEPSC and mIPSC recordings were alternated pseudo-randomly between animals. Histological analysis of ALDH7A1 cKO[Astro] mice was performed in a blinded manner in at least 4 animals per condition. All experiments and analyses in ALDH7A1 cKO[Astro(Mosaic)] mice were performed in a blinded manner containing at least 9 cells from at least 4 separate animals. Cells were selected for imaging in the GCaMP3 channel to blind the experimenter to ALDH7A1 expression. After analysis was complete, expression of ALDH7A1 in each cell was determined by immunohistochemistry by an experimenter blinded to analysis results. Astrocytes located on the surface of the slice, those that had large blood vessels passing through them, or exhibited image registration artifacts were excluded from the dataset. For studies involving the SFN diet (see Sulforaphane diet section below), cages were randomly assigned to receive standard diet or the SFN diet. A specific randomized strategy was not used and no statistical computations were performed to determine sample sizes for most experiments.

Immunohistochemistry: According to established protocol [66,67], mice were perfused with 1X TBS followed by 4% paraformaldehyde (PFA); brains were removed and postfixed in 4% PFA overnight.

38

Antigen retrieval was performed by incubation with L.A.B. solution (Polysciences, Inc.) when necessary: 10 min for 30μm sections, 25 min for 100 μm sections, 1 hour for 250 μm sections. For expression analysis, vibratome sections (30μm) were permeabilized in TBS supplemented with 0.3% Triton X-100, blocked in 5% serum overnight at 4°C with primary antibody, washed in TBS, incubated in secondary antibody + DAPI for 2 hours RT, washed and mounted on Superfrost Plus slides using ProLong Gold antifade reagent. For morphological analysis of astrocytes, 100μm vibratome sections were stained in primary antibody for 2 nights at 4°C followed by 1 night in secondary antibody at 4°C and mounted with Vectashield mounting media with DAPI (Vector Labs H-1200). Acute brain slices used for Ca^{2+} imaging experiments were stained by the same method. For labeling of synaptic proteins, we used a separate protocol. Mice were perfused with TBS supplemented with heparin followed by fresh 4% PFA. Brains were postfixed in 4% PFA overnight at 4°C, washed 3x with TBS, and transferred to 30% sucrose in TBS for 2 days at 4°C. Brains were frozen in 30% sucrose /OCT (2:1) on dry ice for cryoprotection. 20μm sections were cut on a cryostat and stored at -20°C in glycerol/TBS (1:1). Sections were washed with TBS w/0.02% triton-X (TBST; 11332481001 ROCHE) 3x, blocked in TBST w/ 5% goat serum for 1hour, stained at 4°C for 2 nights in primary antibody, washed with TBST, stained in secondary antibody for 2 hours at RT, washed with TBST, and mounted onto slides with Vectashield mounting media with DAPI. Antibodies used: rabbit anti-ALDH7A1 EP1935Y (Abcam 53278; 1:250), chicken anti-GFP (Abcam 13970; 1:2,000), mouse anti-ALDH1L1 (Millipore MABN495; 1:1,000), mouse anti-CC1 (Calbiochem OP80; 1:50), guinea pig anti-NG2 (William Stallcup, Burnham Institute; 1:1,000), goat anti-Iba1 (Novus NB100-1028; 1:250), mouse anti-NeuN (Millipore MAB377; 1:500), mouse anti-GFAP (Millipore MAB360; 1:400), mouse anti-8-oxo-dG (Trevigen 4354-MC-050; 1:250), guinea pig anti-VGAT (synaptic systems 131 004; 1:250), mouse anti-gephyrin (synaptic systems 147 021; 1:500), AlexaFluor 568 anti-IgG1 for gephyrin antibodies, and AlexaFluor 405-, 488-, 568-, 647-conjugated secondary antibodies.

39

Imaging and analysis of fixed tissue sections: Immunofluorescent images were collected on Zeiss 800 and Zeiss 880 confocal microscopes using ZEN Blue/Black software. For ALDH7A1 expression analysis, we collected z-stacks at 20x in three fields of view in prelimbic cortex from four wild-type mice and, for each cell-type marker, counted the percentage cells that co-expressed ALDH7A1. Astrocyte morphological analysis and synaptic puncta analysis followed established protocols [34,68]. For astrocyte morphological analysis, astrocytes within prelimbic cortex were selected for imaging in the GFP channel to blind the experimenter to ALDH7A1 expression. GCaMP3$^+$ astrocytes with no GCaMP3$^+$ neighbors were selected in at least 3 cortical sections from 4 separate mice. Experimenters were unblinded to ALDH7A1 expression after analysis was complete. For measurement of "astrocyte territory volume", 50-70 μm Z-stacks were taken at 63x with 1.3 zoom. Astrocyte fluorescent signal was reconstructed using the surface tool in Imaris Bitplane software. Surface vertices were identified using the MATLAB extension "visualize surface spots". The MATLAB extension "convex hull" was then used to identify the outermost vertices and create a surface render of the outer-rim of each astrocyte, referred to in the text as the "territory volume." For measurement of astrocyte "neuropil infiltration volume" (NIV), 20 μm Z-stacks were taken at 63x with 2.0 zoom. NIV was calculated in Imaris by measuring the total volume of astrocyte processes in 3 randomly placed 13 μm x 13 μm x 10 μm regions of interest within the astrocyte territory containing no DAPI$^+$ cell bodies (e.g. neurons). For synaptic puncta co-localization, we collected 15 slice, 5 μm Z-stacks at 63x with 2x zoom from at least 3 sections for each layer from 8 or more animals per group. Synaptic puncta were determined by colocalization of pre- and post-synaptic markers VGAT and Gephyrin using the ImageJ plugin Puncta Analyzer [69] (written by Bary Wark). Experimenters were blind to the genotype of the animals for imaging and analysis.

Western Blot: Cortical tissue samples were obtained from adult mice following cervical dislocation and cortical dissection, snap frozen in liquid nitrogen, and stored at -80°. "Rest of brain" samples in which the cortices and cerebellum had been removed were also collected in some cases. Protein lysates were prepared by homogenization in lysis buffer (RIPA + protease inhibitors; Roche). For western blots, 20ul of sample containing 20ug of total protein was added to each lane of a Novex 8% Tris-Glycine gel (Life technologies) and run at room temperature followed by transfer to a PVDF membrane. Membranes were blocked for 1hour in 5% milk in PBS + 1% tween, incubated in primary antibody overnight, washed in PBS + tween, incubated in secondary antibody (anti-mouse or anti-rabbit HRP; GE Healthcare) for 1 hour at RT, washed in PBS + tween, incubated with enhanced chemiluminescent substrate (ECL, Pierce), exposed, and quantified using an ImageQuant LAS 4000 mini (GE) digital image acquisition system. Raw images were quantified in ImageJ. Rectangular regions of interest (ROIs) were drawn around selected bands and mean gray value was reported by the measure tool. In each experiment, the same size ROI was used for all bands for every antibody. Background signal was measured by moving the ROI to an empty area of the blot and subtracted from the target signal prior to normalization to loading control signal. Blots were cropped, and in some cases, levels were adjusted for figure clarity. In these cases, image processing was always uniformly applied to all bands for each antibody. Experimenters were blind to the identity of the samples until analysis was complete. Antibodies used: rabbit anti-ALDH7A1 EP1934Y (Abcam 68192; 1:5,000), mouse anti-ALDH1L1 (Millipore MABN495; 1:1,000), mouse anti-GAPDH (Santa Cruz sc-32233, 1:10,000).

Animal behavior: According to established protocol [70,71], behavioral testing was performed in cohorts of 8-15 male mice starting at 10 weeks of age with 1 week between the tests in the following order: Open field test, forced swim test, and seizure threshold test. Separate cohorts were used to assess

41

sucrose preference. Experiments were performed at room temperature. Experimenters were blind to the genotype of the animals during testing and video analysis of the behaviors. Stopwatch+ (Center for Behavioral Neuroscience, Atlanta, GA) was used for video analysis.

Open field test: open field locomotor activity was measured for 120 min in a novel open field box (40 cm x 40 cm; San Diego Instruments, San Diego, CA). Horizontal and vertical locomotor activities in the periphery as well as the center area were automatically recorded by an infrared activity monitor (San Diego Instruments). Single beam breaks were analyzed within 10min bins and are reported as "counts."

Forced swim test: forced swim response was measured by placing the mice in a 5000mL glass beaker half-filled with water. We quantified the percentage of time the mice were actively swimming during the first two minutes.

Seizure threshold test: Each mouse was weighed and administered 40 mg/kg PTZ (i.p., Sigma P6500) and monitored for 30 min. Animals were considered responsive if they developed full tonic-clonic seizures during the 30min trial. Latency to seizure incidence was also measured [72,73].

Acute slice electrophysiology: Mice were anesthetized with Euthasol and perfused intracardially with 15ml ice-cold cutting ACSF (described below). Brains were quickly removed and placed in ice-cold cutting ACSF. Coronal sections (300 µm) containing PFC were prepared in ice-cold cutting ACSF using a vibrating blade microtome (Leica VT1200). Right after cutting, slices were recovered for 10 minutes at 32°C degrees and then transferred to holding ACSF at room temperature. Cutting and recovery were performed with ACSF containing the sodium substitute NMDG (Ting et al., 2014) (in mM): 92 NMDG, 20 HEPES (pH 7.35), 25 glucose, 30 sodium bicarbonate, 1.2 sodium phosphate, 2.5 potassium chloride, 5 sodium ascorbate, 3 sodium pyruvate, 2 thiourea, 10 magnesium, 14 sulfate, 0.5 calcium chloride. ACSF used for holding slices prior to recording was identical, but contained 92 mM

NaCl instead of NMDG and 1 mM MgCl2 and 2 mM CaCl2. ACSF used to superfuse slices during recording contained (in mM): 125 NaCl, 2.5 KCl, 1.25 NaH2PO4, 1 MgCl2, 2.4 CaCl2, 26 NaHCO3, and 11 glucose. All ACSF solutions were saturated with 95% O2 and 5% CO2. For recording, a single slice was transferred to a heated chamber (32°C) and superfused with normal ACSF (2.5 ml min−1) using a peristaltic pump (WPI). Visualization of neurons in L5 of PFC was achieved with an upright microscope equipped for differential interference contrast (DIC) microscopy (BX51WI, Olympus). Whole-cell patch-clamp recordings were made using a MultiClamp 700B amplifier (1 kHz low-pass Bessel filter and 10 kHz digitization) with pClamp 10.3 software (Molecular Devices). Voltage-clamp recordings of mEPSCs were made using glass pipets with resistance 2-4 MOhms, filled with internal solution containing (in mM): 117 cesium methanesulfonate, 20 HEPES, 0.4 EGTA, 2.8 NaCl, 5 TEA-Cl, 2.5 Mg-ATP, and 0.25 Na-GTP, pH 7.2–7.3 and 290 mOsm. mIPSCs were recorded with internal solution containing (in mM): 136 CsCl, 4 NaCl, 1.1 EGTA, 10 HEPES, 0.2 CalCl2, 4 Mg-ATP, 0.3 Na-GTP, pH 7.3 and 290 mOsm. Input resistance was monitored on-line during recordings; cells with access resistance changes greater than 20% were excluded from analysis. Recordings were made at -70mV holding potential and sampled at 1.8 kHz. mEPSCs were pharmacologically isolated by having tetrodotoxin (1 µM), gabazine (1 µM), and APV (50 µM) present throughout the experiment. mIPSCs were pharmacologically isolated with tetrodotoxin (1 µM), DNQX (10 µM), and APV (50 µM). 200-300 events per cell were analyzed, using a threshold of 2X the baseline noise. Analysis of mEPSCs and mIPSCs was performed off-line using the MiniAnalysis program (v 6.0, Synaptosoft) by experimenters blind to the genotype of the animals.

Golgi-Cox staining: We performed Golgi-Cox staining using the FD Rapid Golgi Staining Kit (FD Neurotechnologies, Columbia, MD) following the manufacturer's recommendations. In brief, brains were harvested from adult mice, immersed in impregnation solution for 2 weeks, washed in

cryoprotectant solution for 4 days, and frozen in iso-pentane for storage at -80°C. 100μm thick sections were cut using a cryostat, mounted on slides, incubated in developing solution for 10 min, dehydrated, and coverslipped using permount. For dendritic spine analysis, experimenters were blinded to the genotype of the animals. We selected L2/3 and L5 pyramidal neurons in prelimbic cortex (~Bregma AP +1.9 mm) with processes contained within the plane of the section and visible apical dendrites. Neurons were traced in at least 2 cells in each layer in sections from 4 or more animals per group. For each neuron selected, apical and basal dendrites were manually traced on a Neurolucida Neuron Tracing system (Microbrightfield). Dendritic spines were marked along the primary apical dendrite, all visibly connected secondary apical dendrites, and at least two basal dendrites per cell. Analysis of spine density on each dendritic process subtype and within each cortical layer was performed in Neurolucida Explorer. For analysis of spine density within different cortical layers, segments of the apical dendrites <50 μm were excluded from analysis.

Acute slice calcium imaging: Astrocyte calcium signals from acute brain slices containing prelimbic cortex were prepared, acquired and analyzed using CasCaDe MATLAB code as previously described[40]. Mice were deeply anesthetized with isoflurane and decapitated using a guillotine. Their brains were dissected out and mounted on a vibratome (Leica VT100S) equipped with a sapphire blade. Cortical slices 250 μm thick were cut in ice-cold N-methyl-D-glucamine (NMDG)-based cutting solution containing (in mM): 135 NMDG, 1 KCl, 1.2 KH_2PO_4, 1.5 $MgCl_2$, 0.5 $CaCl_2$, 10 Dextrose, 20 Choline Bicarbonate, (pH 7.4). Cortical slices were then transferred to artificial cerebral spinal fluid (ACSF) containing (in mM): 119 NaCl, 2.5 KCl, 2.5 $CaCl_2$, 1.3 $MgCl_2$, 1 NaH_2PO_4, 26.2 $NaHCO_3$, and 11 Dextrose (292-298 mOsm/L) and were maintained at 37°C for 40 min, and at room temperature thereafter. Both NMDG solution and ACSF were bubbled continuously with 95% O_2/5% CO_2. All slice imaging experiments were performed at room temperature. Fluorescence changes arising from

mGCaMP3 were recorded from individual cortical astrocytes using a Zeiss LSM 710 microscope with a 20x (NA 1.0) water immersion objective (Zeiss), using the 488 nm laser line. GCaMP3$^+$ astrocytes with no GCaMP3$^+$ neighbors were selected for imaging in at least 3 cortical sections from 4 separate mice. Only one cell was imaged in each slice. Slices were continuously superfused with ACSF bubbled with 95% O_2/5% CO_2. Astrocytes were imaged at a laser power of 29 μW, with no pixel averaging, high PMT gain (~800), and with a pinhole size of 2.69 airy units, corresponding to 3.6 μm of z-depth. For each experimental session, individual astrocytes (~3500-4900 μm^2) contained within prelimbic cortex were imaged at the pixel depth of 8 bit with a resolution of 512×512 pixels. Individual imaging sessions consisted of 600 frames at a frame scan rate of 2.1 Hz (0.484 s/frame). Each imaging session consisted of 5 min imaging to control for photoactivation prior to baseline measurements, 5 min baseline measurements, 15 min bath application of 200 nmol tert-butyl hydrogen peroxide (tBHP; Luperox 458139 Sigma) to induce ROS, 5 min imaging after tBHP application. To compensate for minor drift in the XY plane, image stacks were post hoc registered using TurboReg (plugin for ImageJ) for automatic alignment of images. Astrocytes located on the surface of the slice, those that had large blood vessels passing through them, or exhibited image registration artifacts were excluded from the dataset. Following imaging, the relative position of the cell in the section was recorded and a low magnification image was taken to allow the cell to be mapped during post-hoc immunohistochemistry by morphology, laser position, and the relative positions of nearby GCaMP3+ cells. We used the CasCaDe algorithm to identify and extract kinetic information about individual microdomain activity as previously described[40]. Experimenters were blinded to the expression of ALDH7A1 in each astrocyte during imaging and analysis.

Sulforaphane supplementation: Mouse chow containing 600ppm D,L-Sulforaphane (Toronto Research Chemicals, Toronto) was obtained from Research Diets (New Brunswick, NJ). For

45

behavioral and electrophysiology experiments in ALDH7A1 cKO mice, treated mice and littermate controls were placed on a sulforaphane supplemented diet at the time of weaning, at 3 weeks of age. Cages of ALDH7A1 cKO mice and control littermates were randomly assigned to receive standard diet or the SFN diet. The food in the cage feeder was replaced every 7 days with fresh chow that had been stored at 4°C or colder. Each time the food was changed, 21g of diet was added to each cage for every mouse housed in it.

Measurement of sulforaphane in chow: Pellets stored at either 4 ˚C or ~23 ˚C for 0, 6, 14, or 42 days were comminuted into fine powder using a small Krups coffee mill and extracted into 10 volumes of a chilled mixture of equal parts of water, acetonitrile, dimethylformamide, and dimethylsulfoxide. Sulforaphane was measured in these extracts by two separate methods, direct chromatography and cyclocondensation of total isothiocyanates (both free- and conjugated sulforaphane in the feed are captured by the latter method). 1,2-Benzenedithiol was purchased from Alfa Aesar (Cat. No. L11253) and stored at −20 °C. The sulforaphane standard was purchased from LKT Laboratories (Cat. No. S8044). Empower 3 software (Waters) was used for data acquisition.

*Direct Chromatography***:** Extracts were clarified by centrifugation, diluted at least 10-fold in HPLC mobile phase (5% vol:vol tetrahydrofuran in water) then applied to a C18 reverse phase Genesis Lightning, 4.6 x 50 mm, 3 µm HPLC column (Grace Davison Discovery Sciences Cat. No. FM5963E), which was equilibrated with 5% tetrahydrofuran in water and eluted isocratically at 2 mL/min. Elution was monitored at 240 nm (the approximate λ_{max} of sulforaphane). The retention time was determined by comparison with an authentic sulforaphane standard purchased from LKT Laboratories.

*Cyclocondensation***:** Total levels of isothiocyanate equivalents (isothiocyanates plus their metabolites) were measured using the HPLC–based cyclocondensation assay reaction with 1,2-benzenedithiol [74,75]. Isothiocyanates are metabolized to dithiocarbamates *in vivo*, and the cyclocondensation assay detects

46

both isothiocyanates and dithiocarbamates. Briefly, each 2-mL reaction mixture in a 4-mL glass vial contained 100 mM borate buffer (pH 9.2), 16.3 mM 1,2-benzenedithiol, in 50% methanol/50% water. The reaction mixture was incubated for 2 h at 65 °C and, after cooling to room temperature, was centrifuged at low speed to sediment insoluble materials. Aliquots of the supernatant (50 and 100 µL replicates) were analyzed by HPLC, on an ODS C18 Hypersil, 100 x 4.6 mm, 5 µm column (Thermo Scientific #30105-104630). Mobile phase was 80% methanol/20% water, flow rate 0.5 mL/min, and absorbance was monitored at 365 nm as described previously [74,75].

QUANTIFICATION AND STATISTICAL ANALYSIS

Representative immunofluorescent images shown were qualitatively similar across at least 3 animals. Individual data points are displayed for all experiments containing multiple data points. Data are reported as mean ± S.E.M. For Western blot, ALDH7A1 cell-type expression, analysis of inhibitory synaptic puncta density, animal weight, and behavior, *n* represents the number of animals analyzed per condition. For measurements of spine density, whole cell recordings, and experiments in ALDH7A1 cKO$^{Astro(Mosaic)}$ mice, *n* represents the number of cells analyzed per condition and the exact value is provided in the figure legends. The *n* for each experiment is listed in the figure legends. A specific randomization strategy was not used and no statistical computations were performed to determine sample sizes for most experiments. We used sample sizes consistent with other studies in the field. Statistical analyses were performed using GraphPad Prism 8 software. Comparisons of two distributions were calculated by Kolmogorov-Smirnov test. All datasets were assumed to be normally distributed. P-values for two groups were calculated by two-tailed Welch's *t*-test and between three or more groups by one-way ANOVA followed by Tukey's multiple comparison test. Comparisons between genotypes across two conditions were calculated by two-way ANOVA or mixed-model analysis followed by Sidak's multiple comparison tests between genotypes. When multiple

47

measurements were performed in the same animal or cell, we performed a repeated-measure two-way ANOVA followed by Sidak's multiple comparison tests between genotypes. The statistical tests used to measure significance are indicated in each figure along with the corresponding significance level.

DATA AND SOFTWARE AVAILABILITY

All published reagents will be shared on an unrestricted basis. The data that support the findings of this study are available from the corresponding author upon reasonable request. The CasCaDe MATLAB code for analysis of microdomain Ca^{2+} events was previously described and is freely available[40].

Fig. S1. Molecular validation of ALDH7A1 knockout mice.

(A) Gel electrophoresis of polymerase chain reaction products from *Aldh7a1* floxed mice. Bands amplified from floxed (F), wild type (+), and knockout (–) alleles of *Aldh7a1* are indicated.

(B) Adult bodyweight of ALDH7A1 KO^{Global} (KO) mice and wild-type (WT) littermates. No differences were observed (n = 78 WT, 62 KO mice; t_{138} = 0.9770, P = 0.3303)

(C) Locomotor activity of KO mice and WT littermates during an open field test. No differences were observed (n = 11 WT, 14 KO mice; two-way repeated measures ANOVA: genotype $F_{1,23}$ = 0.7110, P = 0.4078; interaction: $F_{23,529}$ = 0.6772, P = 0.8743)

(D) ALDH7A1 immunofluorescence in cortex of ALDH7A1 cKO^{Astro} (cKO) mice. An isolated patch of cortex which retains ALDH7A1 expression is indicated for comparison (arrowhead). Scale bar: 250 µm.

(E) Western blot of ALDH7A1 in tissue homogenates from cortex and non-cortical tissue (rest of brain) from cKO and control (Con) mice. ALDH7A1 expression was reduced in the cortex of cKO mice compared to Con mice, but not as much in the rest of the brain.

All data in (B-C) are represented as mean ± S.E.M.

Fig. S2. ALDH7A1 expression is not heterogeneous across brain regions or sexes.

(A-D) Co-immunostaining of ALDH7A1 with (A) neuronal marker NeuN, (B) microglia marker Iba1, (C) mature oligodendrocyte (OL) marker CC1, and (D) the oligodendrocyte precursor cell (OPC) marker $NG2^+$ in adult mouse cortex. Scale bars: 50 µm. Boxed insets displayed at higher magnification in right three panels. Inset scale bars: 10 µm. ALDH7A1 did not co-localize with these cell-type markers (A-D, arrowheads).

(E-H) ALDH7A1 immunofluorescence (red) in the (E) cerebellum, (F) dentate gyrus, (G) corpus callosum, and (H) olfactory bulb of adult GLT1-eGFP reporter mice. Arrowheads indicate colocalization of ALDH7A1 with GFP in Bergmann glia in (E), adult neural stem cells in (F), fibrous astrocytes in (G), and olfactory bulb astrocytes in (H). Arrows indicate colocalization of ALDH7A1 in velate astrocytes in (E) and hippocampal astrocytes in (F). Scale bars: 100 µm.

(I-J) Western blot of ALDH7A1 in adult cortical tissue of male (♂) and female (♀) mice. Expression is normalized to GAPDH for quantification in (J). No differences were observed (male, $n = 3$ mice; female, $n = 3$ mice; $P = 0.8992$, $t_4 = 0.1349$, two-sided Welch's t-test).

50

Fig. S3. Aspects of excitatory-inhibitory balance are preserved in ALDH7A1 cKO^{Astro} mice.

(A) Frequency of spontaneous excitatory postsynaptic currents (sEPSCs) in layer 5 pyramidal neurons in prelimbic cortex of ALDH7A1 cKO^{Astro} (cKO) mice and controls (Con). No differences were observed (Con, $n = 8$ cells; cKO, $n = 7$ cells; $P = 0.5622$, $t_{11} = 0.5975$, two-sided Welch's t-test).

(B) Amplitude of sEPSCs in layer 5 pyramidal neurons in prelimbic cortex of cKO and Con mice. No differences were observed (Con, $n = 8$ cells; cKO, $n = 7$ cells; $P = 0.1898$, $t_{13} = 1.384$, two-sided Welch's t-test).

(C) Frequency of spontaneous inhibitory postsynaptic currents (sIPSCs) in layer 5 pyramidal neurons in prelimbic cortex of cKO and Con mice. No differences were observed (Con, $n = 12$ cells; cKO, $n = 12$ cells; $P = 0.7983$, $t_{21} = 0.2587$, two-sided Welch's t-test).

(D) Amplitude of sIPSCs in layer 5 pyramidal neurons in prelimbic cortex of cKO and Con mice. No differences were observed (Con, $n = 12$ cells; cKO, $n = 12$ cells; $P = 0.0975$, $t_{14} = 1.777$, two-sided Welch's t-test).

(E) Co-immunofluorence of VGAT and Gephyrin in the prefrontal cortex of cKO and Con mice. VGAT$^+$ Gephyrin$^+$ co-immunopositive puncta indicated (arrowheads). Scale bars: 2 µM.

(F) Quantification of VGAT$^+$ Gephyrin$^+$ puncta density in layer 2/3 and layer 5 of prelimbic cortex in cKO and Con mice. No differences were observed between groups in either layer (Con, $n = 10$ mice; cKO, $n = 8$ mice; Genotype: $P = 0.5805$, $F_{1,16} = 0.2518$; Layer: $P = 0.0020$, $F_{1,16} = 13.53$; Interaction: $P = 0.5805$, $F_{1,16} = 0.3183$; Individuals: $P = 0.0038$, $F_{16,16} = 4.090$; two-way repeated measures ANOVA with Bonferroni post-hoc test: layer 2/3, $P > 0.99$, $t_{32} = 0.2833$; layer 5, $P = 0.9437$, $t_{32} = 0.7281$).

Data in (A-D) and (F) are represented as mean $\pm$ S.E.M.

Fig. S4. ALDH7A1 regulates cortical astrocyte morphology.

(A) Images of ALDH7A1$^+$ and ALDH7A1$^-$ astrocytes (green) and their territory (red) in prelimbic cortex of ALDH7A1 cKO$^{Astro(Mosaic)}$ mice. Scale bar: 10 µm.

(B) Quantification of astrocyte territory volumes in ALDH7A1$^+$ and ALDH7A1$^-$ cells in ALDH7A1 cKO$^{Astro(Mosaic)}$ mice. No differences were observed (ALDH7A1$^+$, n = 12 cells; ALDH7A1$^-$, n = 12 cells; P = 0.5867, t_{21} = 0.5520, two-sided Welch's t-test).

(C) Images of ALDH7A1$^+$ and ALDH7A1$^-$ astrocytes (green) and three neuropil infiltration volumes (NIV; red) from prelimbic cortex of ALDH7A1 cKO$^{Astro(Mosaic)}$ mice. Scale bar: 10 µm. One NIV from each cell (i, ii) is displayed at higher magnification). Scale bar: 2 µm.

(D) Quantification of NIV in ALDH7A1$^+$ and ALDH7A1$^-$ astrocytes in layer 2/3 and layer 5 of prelimbic cortex in ALDH7A1 cKO$^{Astro(Mosaic)}$ mice. NIV was signficantly increased in ALDH7A1$^-$ astrocytes in layer 2/3, but not in layer 5 (Layer 2/3 ALDH7A1$^+$, n = 9 cells; layer 2/3 ALDH7A1$^-$, n = 17 cells; layer 5 ALDH7A1$^+$, n = 19 cells; layer 5 ALDH7A1$^-$, n = 17 cells; Genotype: P = 0.0053, $F_{1,59}$ = 8.369; Layer: P = 0.0835, $F_{1,59}$ = 3.100; Interaction: P = 0.4313, $F_{1,59}$ = 0.6278; two-way ANOVA with Bonferonni's post hoc test: layer 2/3, *P = 0.0411, t_{59} = 2.38; layer 5, P = 0.2048, t_{59} = 1.659).

All data in (B, D) are represented as mean $\pm$ S.E.M.

Fig. S5. ALDH7A1 deletion does not induce astrocyte reactivity.

(A) Co-immunofluorescence of ALDH7A1 (red), ALDH1L1 (green), and mGCaMP3 (pseudocolored magenta) in cortex of adult ALDH7A1 cKO$^{Astro(Mosaic)}$ mice. Scale bar: 20 µM. Insets depict high magnification images of an ALDH7A1$^+$ cell (i) and an ALDH7A1$^-$ cell (ii). Inset scale bars: 5 µM.
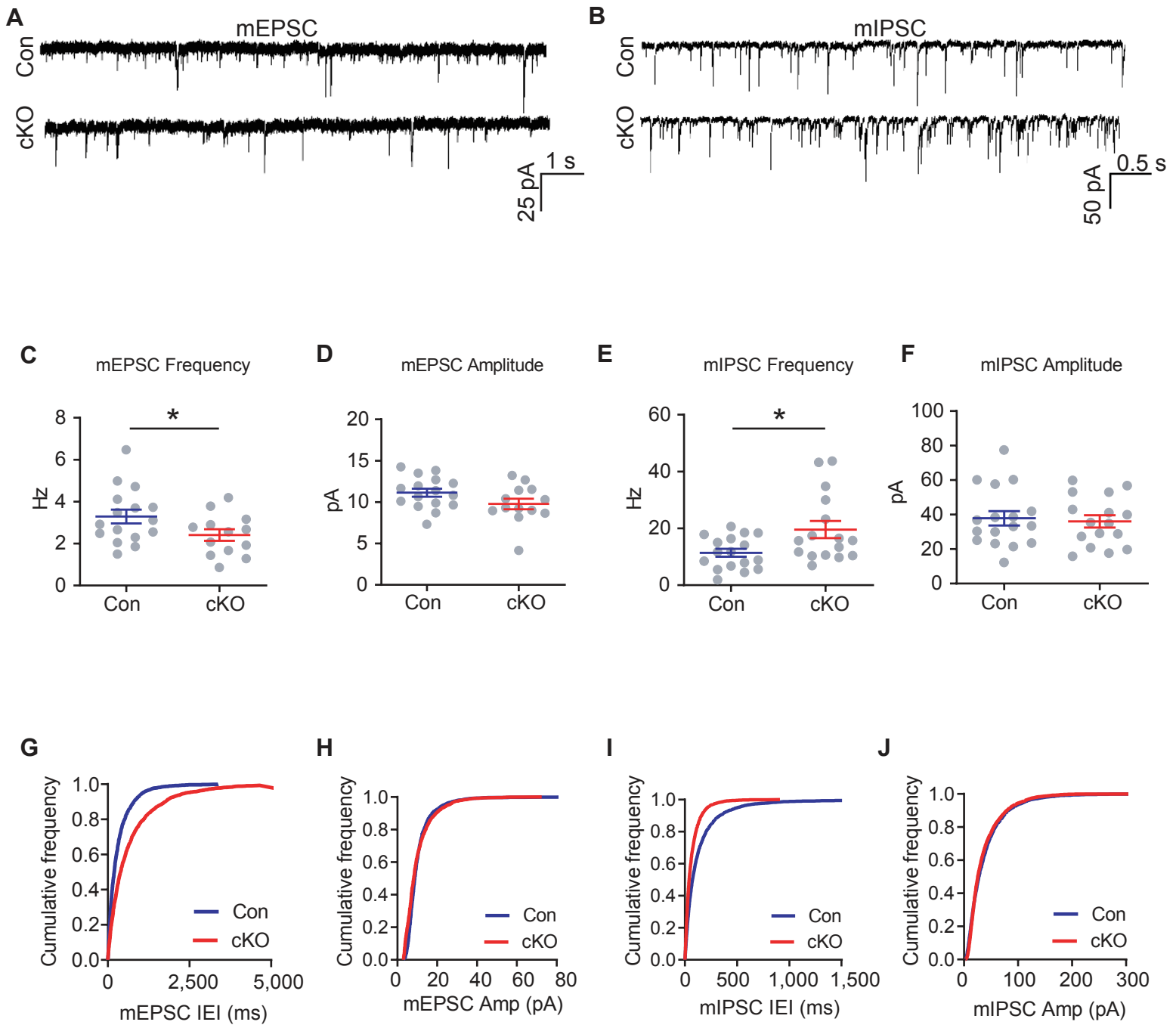
(B) Co-immunofluorescence of ALDH7A1 (red), GFAP (green), and mGCaMP3 (pseudocolored magenta) in cortex of adult ALDH7A1 cKO$^{Astro(Mosaic)}$ mice. Scale bar: 20 µM. Insets depict high magnification images of an ALDH7A1$^+$ cell (i) and an ALDH7A1$^-$ cell (ii). Inset scale bars: 5 µM.

(C) Co-immunofluorescence of ALDH7A1 (red), DNA oxidative stress marker 8-oxo-dG (green), and mGCaMP3 (pseudocolored magenta) in cortex of adult ALDH7A1 cKO$^{Astro(Mosaic)}$ mice. Scale bar: 20 µM. Insets depict high magnification images of an ALDH7A1$^+$ cell (i) and an ALDH7A1$^-$ cell (ii). Nuclear 8-oxo-dG immunofluorescence is highlighted in the astrocyte (arrow) and a cell surrounded by astrocytic processes (arrowhead). Inset scale bars: 5 µM.

Fig. S6. Optimization of SFN diet.

(A) Concentration of SFN in mouse diet pellets stored long-term at 4°C and pellets left at room temperature for 6, 14, and 42 days. Individual data points measured by direct chromatography (%5 THF-HPLC) and by cyclocondensation (CCRxn) are shown.
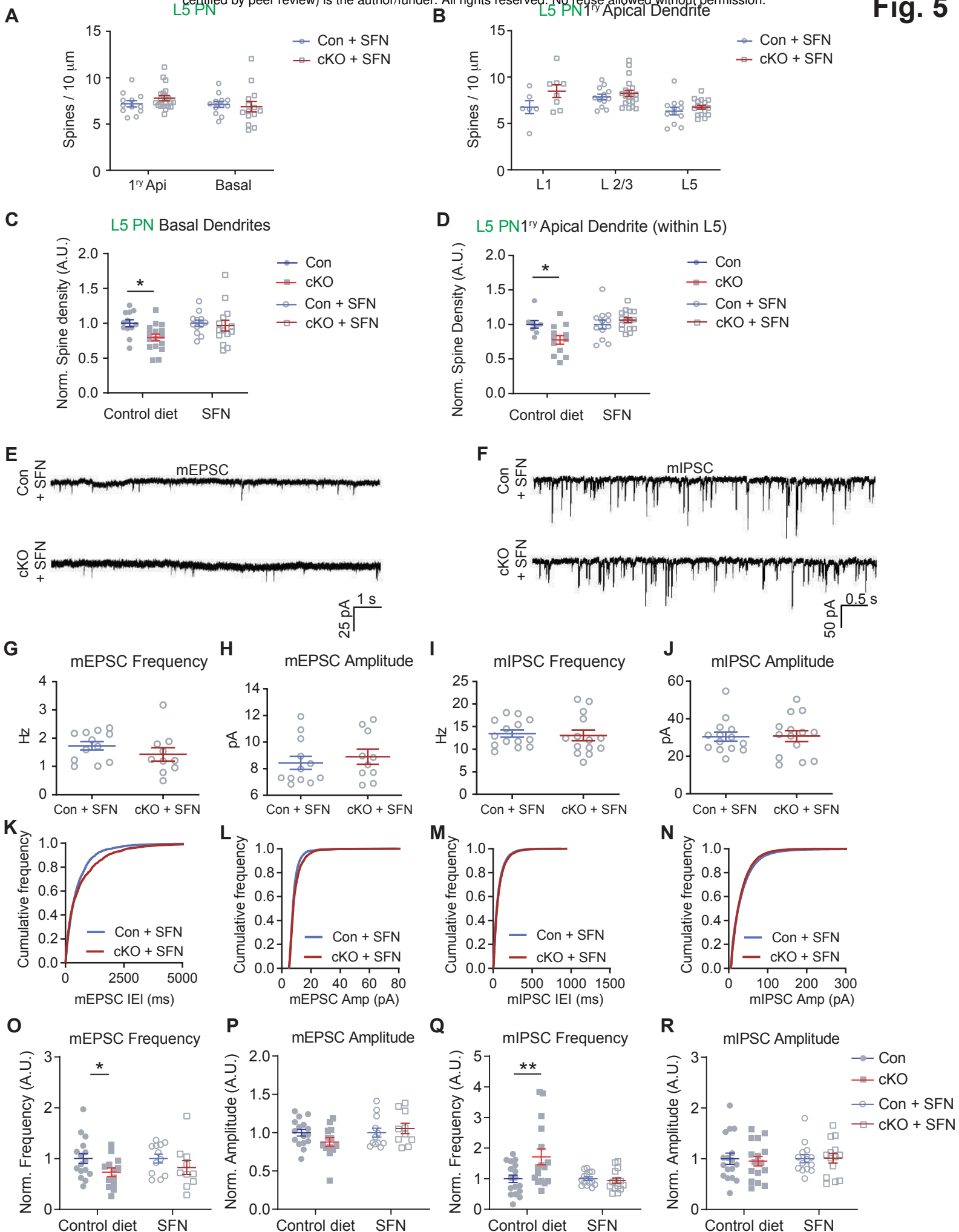
(B) Adult body-weight of ALDH7A1 cKO^{Astro} (cKO) mice and littermate controls (Con) on a standard diet and on a SFN supplemented diet. The diet did not have a significant effect on bodyweight and no differences were detected between cKO and Con mice on either diet (Con:control diet, $n = 15$ mice; Con:SFN diet, $n = 15$ mice; cKO:control diet, $n = 32$ mice; cKO:SFN diet, $n = 15$ mice; Genotype: $P = 0.5934$, $F_{1,64} = 0.2879$; Diet: $P = 0.1005$, $F_{1,64} = 2.777$; Interaction: $P = 0.0679$, $F_{1,64} = 3.448$; two-way ANOVA with Bonferroni post hoc test: control diet, $P = 0.5522$, $t_{64} = 1.098$; SFN diet, $P = 0.2785$, $t_{64} = 1.497$). Data in (B) are represented as mean $\pm$ S.E.M.
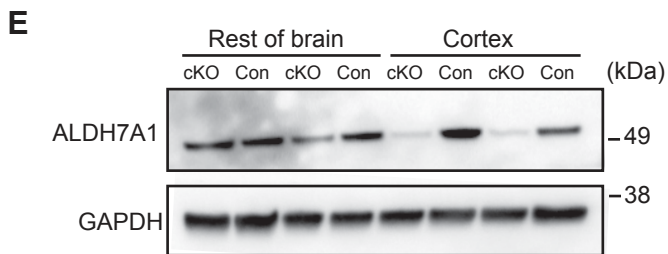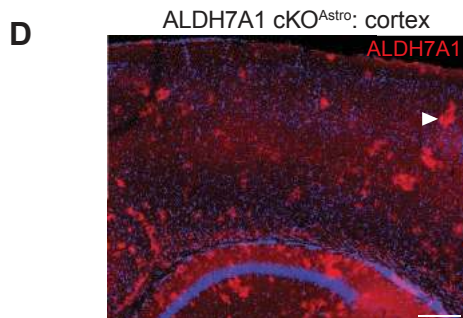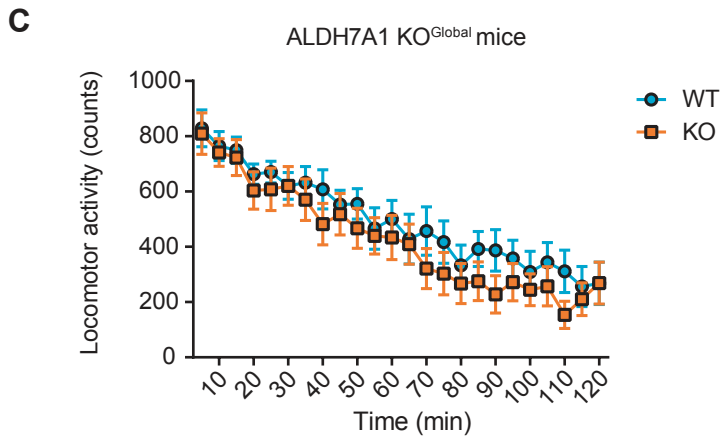
Fig. 1

Fig. 2

Fig. 3

Fig. 4

Fig. 5

Fig 6

Fig. S1

A

500 bp —

396 bp (F)
303 bp (–)
177 bp (+)

+/+ F/+ +/+ F/F F/+ F/F F/– F/F +/– F/F +/– –/–

B

ALDH7A1 KO^{Global} mice

Adult bodyweight (g)

WT   KO

C

ALDH7A1 KO^{Global} mice

Locomotor activity (counts)

Time (min)

WT
KO

D

ALDH7A1 cKO^{Astro}: cortex

ALDH7A1

E

Rest of brain   Cortex
cKO Con cKO Con cKO Con cKO Con (kDa)

ALDH7A1   —49

GAPDH   —38

Fig. S2

Fig. S3

A — sEPSC Frequency

B — sEPSC Amplitude

C — sIPSC Frequency

D — sIPSC Amplitude

E — VGAT / Gephyrin — Con, cKO

F — Inhibitory synapse density

Fig. S4

A

B